AN ANALYTICAL AND NUMERICAL STUDY OF PARAMETRIC RESONANCE IN IMMERSED ELASTIC BOUNDARIES

by

Xin (Simon) Wang

B.Sc., Nankai University, 2001

M.Sc., Nankai University, 2004

A THESIS SUBMITTED IN PARTIAL FULFILLMENT
OF THE REQUIREMENTS FOR THE DEGREE OF
MASTER OF SCIENCE
in the Department
of
Mathematics

SIMON FRASER UNIVERSITY
Summer 2006

APPROVAL

Name: Xin (Simon) Wang

Degree: Master of Science

Title of thesis: An Analytical and Numerical Study of Parametric Resonance in Immersed Elastic Boundaries

Examining Committee:

Dr. J.F. Williams,
Assistant Professor, Mathematics
Simon Fraser University
Chair

Dr. John M. Stockie,
Associate Professor, Mathematics
Simon Fraser University
Supervisor

Dr. Mary Catherine Kropinski,
Associate Professor, Mathematics
Simon Fraser University

Dr. Manfred Trummer,
Associate Professor, Mathematics
Simon Fraser University
SFU Examiner

Date Approved: June 28, 2006

Abstract

We investigate a class of resonant instabilities for fluid-structure interaction problems in which an elastic fiber is immersed in a viscous incompressible fluid. The instabilities are excited via internal forcing driven by periodic variations in the material stiffness. The underlying mathematical model is based on the immersed boundary formalism, which we linearize by assuming small perturbations of the fiber around a flat equilibrium state. The stability analysis makes use of Floquet theory to derive an eigenvalue problem relating the key physical parameters. The resulting solution is much simpler than a similar analysis performed in [8] for a circular fiber geometry, and we show that the results are consistent with this previous analysis. We also uncover an interesting behavior for odd modes, in which forcing by a single odd mode generate instabilities that exhibit a combination of wave numbers, something that is not observed for even wavenumbers. Numerical simulations are presented to verify the analytical results.

Acknowledgments

I would like to thank all those people who made this thesis possible and an enjoyable experience for me.

First of all, I am sincerely grateful to my advisor, Dr. John Stockie, for his supervision and guidance from the very early stage as well as his enthusiasm and patience to answer my questions through out the course of this work. He also provided me unflinching support and extraordinary experience from IB method implementation in engineering applications to conference attendance in CFD.

It is a pleasure to acknowledge the kindness of my advisory committee, Dr. M.C. Kropinski and Dr. M. Trummer, for their time and effort in reviewing this work.

In addition, grateful thanks to Dr. R. Russell and Dr. J.F. Williams for their encouragement of students wishing to pursue research in the field of applied mathematics.

I also wish to express my gratitude to all my friends and colleagues at the Department of Mathematics in SFU, Canada, for their help and friendship.

Finally, I would like to record my deepest gratitude for my entire family during the past years. Among them, I believe I owe deepest thanks to my wife Beibei Li. She always gives me constant understanding and warm love in every situation no matter how dubious my decision were. This thesis could not been accomplished without their supports.

Contents

List of Tables

List of Figures

Chapter 1

Introduction

1.1 Overview

Fluid-structure interaction (FSI) problems have attracted a great deal of interest in recent years. FSI is a multi-physics phenomenon, which involves the interaction of a deformable structure with a fluid. Problems of this type abound in biological, engineering and industrial applications. In engineering, there exist many examples like parachute and airbag dynamics [14], flow in a pipe with elastic walls [35], and a flapping filament in a soap film [41]. In biological fluid dynamics, typical applications include flow of blood in the heart or arteries [31], platelet aggregation during blood clotting [11], swimming of aquatic flagellates [9], and motion of the basilar membrane in the inner ear [2].

The functional interaction between the fluid and solid components leads naturally to a coupled system that poses significant challenges for scientists in terms of proposing physical models, performing computational simulations, and analyzing the equations mathematically. The potential difficulties include the wide variety of possible fluid dynamic effects (compressibility, viscosity, inertia, gravity, turbulence, etc.) with corresponding numerical solvers; the geometric complexity of the solid structure, as well as its time-dependent motion; and the nonlinear interaction at the interface between fluid and solid. Various physical models and computational methods that address these challenges in FSI were reviewed in [10] by Dowell and Hall, and by Mittal and Iaccarino [24].

1.2 Modelling and computational methods

In this work, we consider a fluid-structure interaction problem with the following characteristics. The fluid and structure are treated as two separate subsystems, which are computed independently yet still linked at the interface. One subsystem is a viscous and incompressible fluid which is governed by the Navier-Stokes equations in Cartesian coordinates, fixed in space. The second subsystem is a deformable solid structure, which is immersed in the fluid and represented using Lagrangian variables that move throughout the computation. The structure moves along with the surrounding fluid and changes its configuration continuously in response to the flow. In turn, the solid is elastic and so any deformation exerts body forces back to the surrounding fluid. Hence, there is a *two-way* interaction between the fluid and boundary. This situation is essentially different from traditional exterior problems in engineering fluid dynamics wherein fluid motion occurs through or around a rigid structure with a well-specified geometry.

Amongst the problems involving fluid-structure interactions , there are many examples from the physical world, and in recent decades there have been a wide range of numerical methods developed to simulate them. And among all of these methods, the Immersed Boundary (IB) method has distinguished itself by its ability to deal with very complex deformable boundaries both simply and efficiently. The IB method was originally developed by C.S. Peskin in [26, 27, 29] to simulate blood flow in the heart, and has since then been applied to a wide range of fluid dynamical problems in biology. The method is made up of three main components. First, the Navier-Stokes equations governing the fluid flow are discretized on a fixed Eulerian lattice. Secondly, the immersed solid object is represented in Lagrangian coordinates by a set of moving control points. These two sets of discrete points do not necessarily coincide during the computation, but the evolution of the immersed boundary is constrained such that boundary points move with the fluid according to the *no-slip* boundary conditions. Therefore, the third component is the interaction between the fluid grid points and the immersed boundary points, which is mediated by discrete approximations to Dirac *delta*-functions . A very attractive feature of dealing with the two subsystems separately is that we can discretize the fluid equations by finite-difference methods on a uniform mesh. In this case, the linear system corresponding to the Navier Stokes equations may be solved using a fast solver, i.e., the Fast Fourier Transform (FFT). This is a major advantage of the IB method.

Since 1972 when Peskin first introduced this method, numerous modifications and refinements have been proposed, and now there exist a number of variants of this approach, like the immersed interface method [21], the blob projection method [7], the penalty IB method [15], and so on. Methods in this category have been successfully used for a wide variety of problems including cardiac mechanics [29], cochlear dynamics [2], aquatic animal locomotion [9], and suspensions of flexible filaments [41].

1.3 Developments in analysis

In contrast to the extensive literature on IB computations, relatively few works focus on the analysis of solutions to the equations governing immersed boundaries. Until now, only limited analytical results are available, and these are restricted to simple geometries. Beyer and LeVeque [3] first performed an analysis of a flat fiber in one spatial dimension, where an analysis was performed of the accuracy and stability of the numerical method. Stockie and Wetton [38] investigated the stability of a passive flat fiber in a 2D rectangular geometry, and derived asymptotic decay rates and frequencies using linear analysis. There are also a number of results available for another common geometry: the circular membrane in two dimensions. In [7], a nonlinear analysis for a perturbed circular membrane in inviscid flows was performed by Cortez and Varela. These earlier results corresponded to unforced or passive fibers, while more recently, a linear stability analysis for an actively forced immersed interface was performed by Cortez, Peskin, Stockie and Varela [8]. These authors verified the existence of resonance in a circular membrane wherein the active forcing arose internally from periodic variations in the fiber stiffness parameter.

In this thesis, we continue an emphasis on the study of resonance appearing in an immersed elastic fiber, but instead focus on a perturbed flat fiber, a geometry that has not yet been considered. Because the only forcing in this problem is internal, through a time-dependent stiffness parameter, any resonance that appears is called "*parametric resonance*". In fact, parametric resonance is distinct from the usual resonance that arises from an external forcing term in the following two ways:

- parametric resonance can lead to unbounded oscillations in the solution *even in the presence of damping*, which is not the case for externally forced problems; and
- the resonant response to a system that is parametrically forced is at twice the forcing

frequency, in contrast with externally forced system where the response is close to the same frequency as the forcing.

A previous paper of Cortez and his colleagues [8] has analyzed the parametric resonance phenomenon in a circular geometry, which gives rise to complex Bessel functions. This thesis performs a similar analysis for a flat fiber which is useful for considering problems where the geometry is not circular. We will see later on that the analytical solutions in this case are considerably simplified owing to the elimination of the Bessel functions, but the results are otherwise consistent with [8]. One of the advantages of this simplification is that the analytical technique, based on Floquet theory, is particularly easy to understand. We have also uncovered an unusual behaviour in the resonant behaviour of odd-numbered modes which differs from that observed in even wavenumbers, which as far as we know has not yet been reported in the literature.

1.4 Chapter organization

The thesis is organized as follows. In Chapter 2, we present the mathematical structure of the immersed boundary method for a flat elastic fiber immersed in a viscous incompressible fluid, and describe two alternative IB formulations for the problem: one in terms of *delta*-functions, and the other where singular forces are eliminated in favor of stress jump conditions across fiber. In Chapter 3, a linearized IB formulation in terms of jump conditions across the interface is derived for a flat boundary, which is excited by periodic internal forcing through the stiffness parameter. We employ Floquet analysis to obtain an eigenvalue problem which defines a relationship between the amplitude of the perturbation and the wavenumber, and use these results to draw conclusions about the resonant instabilities in the fiber. Chapter 4 contains details of the discrete scheme proposed in [26, 29], as well as corresponding numerical solution algorithms. In Chapter 5, several numerical simulations are presented to validate the results of the Floquet analysis, as well as the convergence of the IB method.

Chapter 2

Mathematical Formulation

2.1 General IB model

We propose in this thesis to consider an immersed boundary that is a flat, elastic fiber which extends to infinity, and is immersed in a viscous incompressible flow. We restrict ourselves to two dimensions so that the fiber is a line which at equilibrium sits along the x-axis. We are interested ultimately only in small spatially-periodic oscillations (Fourier modes) and so we restrict ourselves to the rectangular domain $\Omega(x, y) = [0, L] \times [-L/2, L/2]$ and apply periodic boundary conditions on all sides. Then, this situation corresponds to a periodic array of horizontal fibers that extends to infinity in both vertical directions.

The immersed elastic fiber is represented by $\Gamma(t)$, and is assumed to be massless and incompressible. The restoring force exerted by deforming any two nearby points on the fiber is taken to be analogous to that of a linear spring with zero resting length. Therefore, in the absence of external forcing, any finite section of the fiber would shrink to a point. In our periodic geometry, the fiber remains always under tension and will stay at the equilibrium location $y = 0$ in the absence of any perturbation.

If small perturbations are introduced in the fiber's position, the fiber will begin to oscillate around its equilibrium and the amplitude will gradually decrease to zero (owing to viscous damping forces in the fluid) until the fiber again lies along the x-axis. In turn, the restoring forces within the fiber will affect the pattern of the flow on either side of the fiber, $\Omega^{\pm}$. Also, because of the incompressibility condition, it is not possible for the fiber to intersect itself and so the fiber will always divide the domain into two sub-domains, Ω^{+} and Ω^{-}. In summary, the model is described as Fig. 2.1.

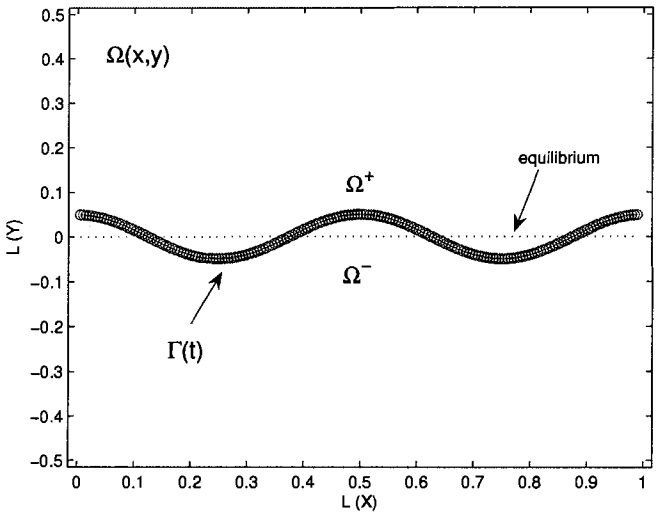

Figure 2.1: The two-dimensional model: an elastic flat fiber immersed in the fluid. The fiber is perturbed away from its equilibrium state initially and acts as an interface $\Gamma(t)$ to separate the domain $\Omega(x,y)$ into two parts $\Omega^{\pm}$.

The fluid is parameterized in terms of Cartesian coordinates $\mathbf{x} = (x,y) \in \Omega$ as well as time $t \in (0,T]$ and we denote the relevant fluid quantities for velocity as $\mathbf{u}(\mathbf{x},t)$, pressure $p(\mathbf{x},t)$ and fluid body force $\mathbf{f}(\mathbf{x},t)$. The fluid motion is governed by the viscous incompressible Navier-Stokes equations

$$\rho\left(\mathbf{u}_t + \mathbf{u}\cdot\nabla\mathbf{u}\right) = \mu\triangle\mathbf{u} - \nabla p + \mathbf{f}, \tag{2.1}$$

$$\nabla\cdot\mathbf{u} = 0, \tag{2.2}$$

where the constants ρ and μ are the fluid density and viscosity.

The immersed elastic fiber is represented in Lagrangian variables using a curvilinear coordinate s which parameterizes the fiber. The choice of the fiber parametrization is somewhat arbitrary, and so we will select s to lie in the interval $[0,1)$, after the non-dimensionlization in the next section. At time t, the configuration of the fiber is described by a set of control points $\mathbf{X}(s,t)$ in Lagrangian variables and $\mathbf{F}(s,t)$ corresponds to the force density of immersed boundary.

Using this notation, the interaction between the fluid and the immersed boundary will be represented in two separate equations, which couple the fluid and fiber and transfer the key physical quantities (namely, velocity and force) between them. First of all, since the

fluid and fiber together satisfy the *no-slip* boundary condition at the interface, the velocity of the fiber must be given as

$$\frac{\partial \mathbf{X}}{\partial t} = \mathbf{u}(\mathbf{X}(s,t),t) = \int_{\Omega} \mathbf{u}(\mathbf{x},t)\delta(\mathbf{x} - \mathbf{X}(s,t))d\Omega. \tag{2.3}$$

Secondly, any deformation of the elastic fiber introduces a corresponding contribution to the fiber force density, which is then distributed to the surrounding flow, which we can write as the following convolution:

$$\mathbf{f}(\mathbf{x},t) = \int_{\Gamma} \mathbf{F}(s,t)\delta(\mathbf{x} - \mathbf{X}(s,t))ds. \tag{2.4}$$

It is clear that in the interactions between the fluid and fiber in (2.3)-(2.4), the Dirac delta function $\delta(\mathbf{x})$ plays an important role. It is important to note that the delta functions above are two-dimensional delta functions $\delta(\mathbf{x}) = \delta_1(x)\delta_2(y)$. Later we will see that the numerical approximations to the delta function is an essential part of the IB method.

We now have four equations describing the FSI problem in hand, but are still missing a definition of the fiber force density $\mathbf{F}(s,t)$. In the natural world, there exist a variety of linear *and* non-linear elastic forces within deformable solids. As is usual in immersed boundary simulations, we choose here to study the simplest forcing of linear models, using Hooke's Law for linear springs. In addition, we assume that the only source of Lagrangian forcing arises from stretching of the fiber and that there are no bending or surface tension forces. Hooke's law for the tension force $T(s,t)$ within the fiber can be written

$$T = \kappa \left(\left| \frac{\partial \mathbf{X}}{\partial s} \right| - 1 \right), \tag{2.5}$$

where $\kappa(s,t)$ denotes the stretching stiffness, which may be a constant, but could in general depend on the both the fiber location s and time t. In this thesis, we are particularly interested in the parametric resonance of an immersed boundary wherein the stiffness is restricted to be a function of time only, $\kappa(t)$. In particular, we take

$$\kappa(t) = \kappa_c(1 + 2\epsilon \sin(\omega_0 t)), \tag{2.6}$$

where κ_c is a stiffness constant, ω_0 is the modulating frequency, and ϵ denotes an amplitude parameter. Our model excludes the cases with spatially varying stiffness. Nonetheless, such cases do exist in natural biological organs such as the basilar member in the inner ear, which has a stiffness that is known to vary exponentially along its length.

In order to express the force density, we first need to define the unit tangent vector to the immersed boundary,

$$\boldsymbol{\tau} = \frac{\partial \mathbf{X}}{\partial s} \Big/ \left| \frac{\partial \mathbf{X}}{\partial s} \right|. \tag{2.7}$$

Together with (2.5)-(2.6), the local force density per unit length is then given by

$$\mathbf{F}(s,t) = \frac{\partial}{\partial s} \left(T\boldsymbol{\tau} \right). \tag{2.8}$$

See Peskin [28] for a derivation. Noting that the resting length of the fiber is equal to zero, we can obtain the fiber force density as

$$\mathbf{F}(s,t) = \left(\kappa \mathbf{X}_s \right)_s, \tag{2.9}$$

which depends linearly on the fiber configuration $\mathbf{X}$. The force (2.9) points purely in the normal directions, and can be reduced from (2.8) too by substituting (2.5) and (2.7) in it and setting the resting length to zero. According to our earlier assumptions, the thickness and mass of the fiber are negligible; hence, we ignore the effects of gravity and buoyancy of the structure, and so the fluid body force $\mathbf{f}(\mathbf{x},t)$ arises solely from the integral of the fiber force density in (2.4).

In conclusion, equations (2.1)-(2.4) and (2.9), represent a coupled system that describes the motion of the fluid and fiber. These equations will be discretized in Chapter 4.

2.2 Non-dimensionalization

For the purpose of the stability analysis in the next Chapter, and in the interests of reducing the number of physical parameters, we non-dimensionalize the system by scaling the variables as follows

$$\begin{aligned}
\widetilde{\mathbf{x}} &= \frac{\mathbf{x}}{L}, \\
\widetilde{\kappa} &= \frac{\kappa}{\kappa_c}, \\
\widetilde{t} &= t\omega_0, \\
\widetilde{\mathbf{u}} &= \frac{\mathbf{u}}{U_0}, \\
\widetilde{p} &= \frac{p}{\rho U_0 \omega_0},
\end{aligned}$$

where variables with a tilde are dimensionless. The last two expressions are based on the following scale for the velocity

$$U_0 = L\omega_0.$$

Now we apply these scalings to the IB formulation in Section 2.1, and derive an equivalent system in dimensionless form

$$\mathbf{u}_t + \mathbf{u}\cdot\nabla\mathbf{u} = \nu\triangle\mathbf{u} - \nabla p + \sigma\,\mathbf{f}, \tag{2.10}$$

$$\nabla\cdot\mathbf{u} = 0, \tag{2.11}$$

$$\mathbf{f}(\mathbf{x},t) = \int_0^1 \mathbf{F}(s,t)\delta(\mathbf{x}-\mathbf{X})\,ds, \tag{2.12}$$

$$\mathbf{X}_t = \mathbf{u}(\mathbf{X},t) = \int\int_{[0,1]^2} \mathbf{u}(\mathbf{x},t)\delta(\mathbf{x}-\mathbf{X})\,d\Omega, \tag{2.13}$$

$$\mathbf{F}(s,t) = \kappa\frac{\partial^2\mathbf{X}}{\partial s^2}. \tag{2.14}$$

In terms of dimensionless variables, the time-dependent stiffness introduced above becomes

$$\kappa = \kappa(s,t) = 1 + 2\epsilon\sin t. \tag{2.15}$$

From now on, we will deal with only dimensionless variables and so we will drop the tilde notation.

By considering the IB model in dimensionless form we obtain some advantage. For example, the computational domain has been transformed to a standard unit square $[0,1]^2$. Also, the physical parameters appearing in the PDE system have been reduced to two dimensionless parameters only,

$$\nu = \frac{\mu}{\rho U_0 L}, \qquad \sigma = \frac{\kappa_c}{\rho U_0^2}, \tag{2.16}$$

where ν is the reciprocal of the Reynolds number and σ the square of the ratio of the natural and driving frequencies.

2.3 Jump condition formulation

In the dimensionless system (2.10)-(2.16), the singular nature of the delta functions can frustrate the analysis. So it is more convenient to introduce an alternate formulation in terms of jump conditions across the fiber. This formulation of the IB method in terms of

jumps has been used before by Stockie and Wetton [38] to investigate IB stability, and by LeVeque and Li [21] to develop the immersed interface method.

In general, solutions of the fluid equations in (2.10) and (2.11) will be continuous on either side of the immersed interface. However, they may be discontinuous or non-smooth when crossing the fiber owing to the singular distribution of the fluid body force $\mathbf{f}(\mathbf{x}, t)$ in (2.12). These discontinuities in the solution or its derivatives are what give rise to the jump conditions at the interface. Please refer to the literature [19, 22, 18] for more details about the derivation of those jump conditions.

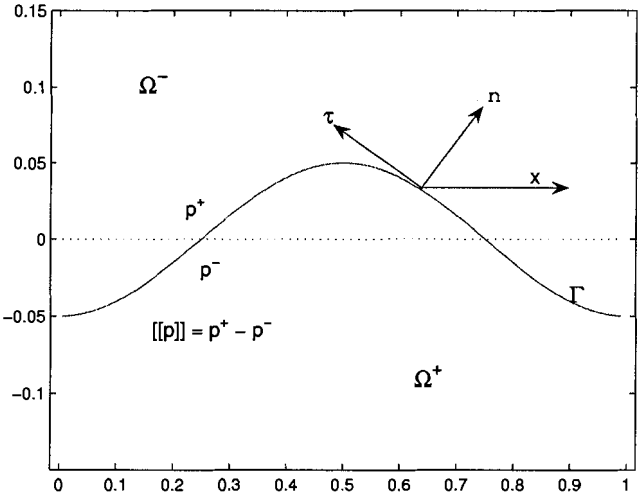

Figure 2.2: An illustration of the jump conditions across the interface, e.g. the pressure $[[p]]$. Also the normal $\mathbf{n}$ and tangent $\boldsymbol{\tau}$ vectors are given at one point of the interface Γ.

Since the immersed fiber is assumed to satisfy *no-slip* boundary conditions, no fluid can pass through. Some quantities are continuous across the interface, such as the velocity $[[\mathbf{u}]] = 0$, where $[[\cdot]] = (\cdot)|_{\Gamma_+} - (\cdot)|_{\Gamma_-}$ denotes the difference between a physical quantity on either side of the boundary. In addition to the tangent vector $\boldsymbol{\tau}$ as defined in (2.7), we denote the normal vector by $\mathbf{n}$, at each physical point in the boundary $\Gamma(t)$, as shown in Fig. 2.2.

Because of the singular forces, the derivatives of velocity and the pressure may be discontinuous across the interface, and obey the following jump conditions

$$\nu\,\boldsymbol{\tau}\cdot[[\mathbf{n}\cdot\nabla\mathbf{u}]] = -\sigma\,\boldsymbol{\tau}\cdot\left(\frac{\mathbf{F}(s,t)}{|\frac{\partial\mathbf{X}}{\partial s}|}\right), \tag{2.17}$$

$$-[[p]]+\nu\,\mathbf{n}\cdot[[\mathbf{n}\cdot\nabla\mathbf{u}]] = -\sigma\,\mathbf{n}\cdot\left(\frac{\mathbf{F}(s,t)}{|\frac{\partial\mathbf{X}}{\partial s}|}\right), \tag{2.18}$$

where $\left(\mathbf{F}(s,t)/|\frac{\partial\mathbf{X}}{\partial s}|\right)$ gives the force per unit length measured at each boundary point. Further simplification can give rise to the second equation (2.18), if we notice the impressibility (2.11) in Navier-Stokes equations. It follows that the term $\mathbf{n}\cdot[[\mathbf{n}\cdot\nabla\mathbf{u}]] = 0$ will disappear automatically.

At this point, we have now eliminated the delta functions appearing in the Section 2.2 by three jump conditions, which link the fluid and fiber across the interface. The resulting "jump" system will be used to analyze the stability of immersed fiber in Chapter 3

$$\mathbf{u}_t+\mathbf{u}\cdot\nabla\mathbf{u} = \nu\triangle\mathbf{u}-\nabla p, \tag{2.19}$$

$$\nabla\cdot\mathbf{u} = 0, \tag{2.20}$$

$$\mathbf{X}_t = \mathbf{u}(\mathbf{X}(s,t),t), \tag{2.21}$$

$$[[\mathbf{u}]] = 0, \tag{2.22}$$

$$\nu\,\boldsymbol{\tau}\cdot[[\mathbf{n}\cdot\nabla\mathbf{u}]] = -\sigma\,\frac{\mathbf{F}(s,t)\cdot\boldsymbol{\tau}}{|\frac{\partial\mathbf{X}}{\partial s}|}, \tag{2.23}$$

$$-[[p]] = -\sigma\,\frac{\mathbf{F}(s,t)\cdot\mathbf{n}}{|\frac{\partial\mathbf{X}}{\partial s}|}. \tag{2.24}$$

The expressions for the linear force density (2.14) and time-dependent stiffness (2.15) complete the jump formulation of the IB method.

Chapter 3

Stability Analysis

In contrast with the large body of literature on numerical simulations for immersed boundary problems, relatively few publications have appeared that analyze the stability or other properties of solutions to the IB equations. The first paper to perform such an analysis was by Beyer and LeVeque [3], where they studied the IB model in one spatial dimension and analyzed the numerical method to show the limitations of the IB method in terms of accuracy due to the choice of discrete delta function. Their results demonstrated that it was possible to optimize the spatial accuracy using an appropriate approximate delta function. For two dimensional problems, it is much more of a challenge to derive general results regarding solutions of the IB equations owing to complications from geometry and the singular nature of the applied forces.

Up to this point, analytical results have been limited to problems with simple geometry. For example, Cortez and Varela performed a nonlinear analysis for a perturbed circular membrane in inviscid flow [7]. Their immersed structure was passive, and only generated forces under elastic deformation in response to the motion of surrounding flow. Several years later, Cortez and colleagues investigated the stability of the viscous case for both a passive and active circular membranes [8]. In this work, the fiber was excited via a time-dependent internal forcing appearing as a periodic variation of the fiber stiffness parameter. This situation is a prototype for problems which abound in biological applications such as the beating heart and flagellated cells.

Besides the circular membrane, another important configuration to consider is a flat fiber, which also appears in many applications such as the basilar membrane in the inner ear [2], suspended pulp fibers [37], and flapping filaments [41]. An analysis of the stability

of perturbations to a flat fiber in two dimensions was studied by Stockie and Wetton in [38]. In this paper, the authors investigated the linear stability of the fluid-fiber interaction under small sinusoidal perturbations and obtained asymptotic expansions of the resulting frequency and decay rates for the excited modes of oscillation.

There has as yet been no attempt to extend the results of Cortez et al. [8] to consider a flat fiber subjected to internal parametric forcing. In this thesis, we will address this issue and analyze the stability of a flat fiber immersed in a viscous incompressible Navier-Stokes flow. We will see that the parametrically forced system can give rise to resonance, in the sense that the amplitude of oscillation in the linearized system can become unbounded even in the presence of viscous damping. These results show that the flat fiber exhibits very similar behavior to the circular fiber considered in [8].

3.1 Linearization

According to the description in Chapter 2, we consider a flat immersed boundary which has an equilibrium state along x-axis ($y = 0$) initially, and the resting length is $L = 1$ (in the non-dimensional system). A perturbation to the equilibrium state is introduced and represented in Eulerian variables as $(\xi(s,t), \eta(s,t))$ so that the perturbed fiber position is given by

$$\mathbf{X}(s,t) = (s + \xi(s,t),\, \eta(s,t))\,, \tag{3.1}$$

where $s \in [0,1)$. The perturbations ξ and η are understood to be small and are assumed to have continuous derivatives up to second order. Following the development in [36], we aim next to perform asymptotic expansions and omit higher order terms in ξ and η.

First of all, we need to derive some basic linearized quantities for later use. The unit stretching length $\left|\frac{\partial \mathbf{X}}{\partial s}\right|$ involved in the jump conditions (2.23) and (2.24) is approximated from (3.1) expanding in a Taylor series and neglecting higher order (non-linear) terms in ξ, η and their derivatives:

$$\begin{aligned}
\frac{\partial \mathbf{X}}{\partial s} &= (1 + \xi_s, \eta_s)\,, \\
\left|\frac{\partial \mathbf{X}}{\partial s}\right| &= \sqrt{(1+\xi_s)^2 + (\eta_s)^2} \\
&\approx \sqrt{1 + 2\xi_s} \\
&\approx 1 + \xi_s.
\end{aligned}$$

Similarly, based on the definition (2.7), we obtain linear approximations for the tangent and normal vectors

$$\begin{aligned} \boldsymbol{\tau} &\approx \left(1, \frac{\eta_s}{1+\xi_s}\right) \approx (1, \eta_s)\,, \\ \mathbf{n} &\approx (-\eta_s, 1)\,. \end{aligned}$$

Next, we will derive the linearized version of the jump formulation of the IB equations. We start by linearizing the force density. As we discussed earlier, we will consider internal forcing through a periodically varying stiffness parameter $\kappa(t)$ in (2.15). By substituting the perturbed fiber position (3.1) into the non-dimensionalized force density (2.14), the linearized form of the fiber force is given as

$$\mathbf{F}(s,t) = \kappa \cdot (\xi_{ss}, \eta_{ss})\,. \tag{3.2}$$

For the purposes of convenience to our analysis, the stiffness $\kappa(t)$ is rewritten in terms of complex variables as

$$\kappa(t) = 1 - i\epsilon e^{it} + i\epsilon e^{-it}. \tag{3.3}$$

Next, we will treat the jump conditions in IB formulation in a similar way. The condition (2.24) involves the difference in pressure p across the fiber, which is related to the normal component of force density per unit length. Using the above expressions, we linearize the pressure jump as follows

$$-[[p]] = -(\sigma\kappa) \cdot \eta_{ss}. \tag{3.4}$$

In the tangential jump condition (2.23), the nonlinear term $[[\eta_s \frac{\partial u}{\partial x}]]$ is negligible in comparison to $[[\frac{\partial u}{\partial y}]]$ in the jump $[[\mathbf{n} \cdot \nabla \mathbf{u}]]$. Once we take the tangential component of this jump, $\boldsymbol{\tau} \cdot [[\frac{\partial \mathbf{u}}{\partial y}]]$, the contribution from the component of horizontal velocity $[[\frac{\partial u}{\partial y}]]$ is more significant than that of the vertical one $\eta_s[[\frac{\partial v}{\partial y}]]$. Therefore, the left hand side of this jump condition will be dominated by the derivative of the horizontal velocity with respect to vertical variable. The condition (2.23) then reduces to

$$\nu \cdot [[\frac{\partial u}{\partial y}]] = -(\sigma\kappa) \cdot \xi_{ss}. \tag{3.5}$$

The last two jump conditions expressing continuity of the velocity across the fiber remain unchanged:

$$\begin{aligned} [[u]] &= 0, \\ [[v]] &= 0. \end{aligned} \tag{3.6}$$

We next consider the equation (2.21) which governs the evolution of the fiber. Using Taylor expansions, it can be simplified as

$$\frac{\partial \mathbf{X}}{\partial t} = \mathbf{u}\left(s+\xi(s,t),\eta(s,t),t\right) \tag{3.7}$$

$$\approx \mathbf{u}\left(s,0,t\right). \tag{3.8}$$

Finally, we would like to linearize the Navier-Stokes equations (2.19) by ignoring the nonlinear inertial term $\mathbf{u}\cdot\nabla\mathbf{u}$ while still retaining the time derivative $\mathbf{u}_t$, which yields the unsteady Stokes equation:

$$\mathbf{u}_t = \nu\triangle\mathbf{u} - \nabla p, \tag{3.9}$$

$$0 = \nabla\cdot\mathbf{u}. \tag{3.10}$$

Our use of the unsteady Stokes equations (as opposed to simply the steady Stokes equations) requires some justification, since it is more often the case that both inertial terms are of similar magnitude and so must be dropped together. In the previous chapter, we chose to base our velocity scale $U = L\omega_0$ on the fiber forcing frequency, which is not necessarily representative of the actual fluid velocity engendered by the fiber motion. If we leave the velocity scale undetermined for the moment, then the Navier-Stokes equations (2.19) can be written in non-dimensional variables as:

$$\frac{\beta}{Re}\mathbf{u}_t + \mathbf{u}\cdot\nabla\mathbf{u} = \frac{1}{Re}\triangle\mathbf{u} - \nabla p,$$

where $Re = \frac{\rho UL}{\mu} = \frac{1}{\nu}$ is the *Reynolds number*, and $\frac{1}{\beta} = \frac{\mu T}{\rho L^2}$ is the *Stokes number*, based on the time scale $T = \frac{1}{\omega_0}$. In computations reported later in Chapter 5, we compute values of the fluid velocity which can be used to determine that the ratio $\frac{\beta}{Re} = L\omega_0/U$ (which is known as the *Strouhal number*) typically lies in the range $[10, 10^2]$; hence, it is clearly not the case that the two inertial terms are of equal size and so we are justified in dropping only the nonlinear inertial term. We will therefore consider the unsteady Stokes equation (3.9) in the remainder of this work.

In conclusion, the linearized version of the IB equations includes the following components. The elastic fiber, under small perturbations, evolves according to (3.7). The fluid is divided into two sub-domains by the immersed boundary, which are separately governed by unsteady Stokes' equations (3.9) and (3.10). Moreover, four interfacial jump conditions (3.4)-(3.6) are given in the linearized form and help to link two subdomains of the fluid separated by the immersed fiber $\Gamma(t)$ as shown in Fig. 2.1 and Fig. 2.2.

3.2 Fourier transformation

We can now move on to our primary goal of demonstrating the existence of parametric resonance in the immersed boundary. That is to say, we will show that the fiber becomes unstable owing to the periodic internal forcing in the stiffness parameter (3.3). Naturally, we want to predict instabilities by looking for a relationship between wave modes $\wp$ and oscillation amplitude ϵ, with respect to given system parameters ν and σ in (2.16). Our analysis is based on a general approach from the Floquet theory. Many problems in fluid mechanics have been studied by applying similar procedures, such as the horizontal interface between two fluids with different densities [17], the previous analysis of parametrically forced circular elastic membranes immersed in fluid [8]. Our work here will parallel the methods in these two publications. Finally, we will see that the eventual results yield similar stability diagrams to those presented in [8].

We assume that solutions to the linearized IB system can be expanded in the form of Fourier series as follows

$$\begin{aligned}
u(x,y,t) &= e^{i2\pi\wp x} \sum_{n=-\infty}^{\infty} \widehat{u_n}(y)\, e^{(\lambda+in)t}, \\
v(x,y,t) &= e^{i2\pi\wp x} \sum_{n=-\infty}^{\infty} \widehat{v_n}(y)\, e^{(\lambda+in)t}, \\
p(x,y,t) &= e^{i2\pi\wp x} \sum_{n=-\infty}^{\infty} \widehat{p_n}(y)\, e^{(\lambda+in)t}, \\
\xi(s,t) &= e^{i2\pi\wp s} \sum_{n=-\infty}^{\infty} \widehat{\xi_n}\, e^{(\lambda+in)t}, \\
\eta(s,t) &= e^{i2\pi\wp s} \sum_{n=-\infty}^{\infty} \widehat{\eta_n}\, e^{(\lambda+in)t},
\end{aligned} \tag{3.11}$$

where $i = \sqrt{-1}$ is the imaginary unit, $\wp \geq 1$ is the integer wavenumber, and $e^{\lambda t}$ is the *Floquet multiplier* with the complex number $\lambda := \alpha + i\beta$ (α and β are assumed real).

Then we apply the transformation (3.11) to the fluid equations (3.9) and (3.10) so as to obtain relationships for the Fourier coefficients. For example, from the incompressibility condition (3.10), we obtain the following equation

$$(i2\pi\wp)\,\widehat{u_n}(y) + \frac{d}{dy}\widehat{v_n}(y) = 0, \tag{3.12}$$

which defines a relationship between the Fourier coefficients $\widehat{u_n}(y)$ and $\widehat{v_n}(y)$ that is satisfied for any indices n. Here, we will use (3.12) as a constraint to cancel out the unknowns $\widehat{u_n}$ and $\widehat{v_n}$ in the system that is obtained by applying the Fourier transformation (3.11) to the fluid momentum equations (3.9). It gives a second order ordinary differential equation

(ODE) with respect to the pressure coefficient $\widehat{p_n}(y)$ as follows

$$\frac{d^2\widehat{p_n}}{dy^2} - (2\pi\wp)^2\widehat{p_n} = 0. \tag{3.13}$$

When taken together with boundedness conditions at infinity, $y \to \pm\infty$, solutions of the pressure are given on both sides "$\pm$" of the fiber in terms of

$$\widehat{p_n}^{\pm}(y) = A_n^{\pm} e^{\mp(2\pi\wp)y}, \tag{3.14}$$

where $A_n^{\pm}$ are as yet undetermined constants.

We next substitute the pressure solutions (3.14) into the transformed momentum equations from (3.9) to obtain another two ODEs involving the velocity Fourier coefficients $\widehat{\mathbf{u}_n}$. By imposing the same boundedness conditions as before, we have

$$\begin{aligned} \widehat{u_n}^{\pm}(y) &= B_n^{\pm} e^{\mp\theta y} - \tfrac{i2\pi\wp}{\lambda+in} A_n^{\pm} e^{\mp(2\pi\wp)y}, \\ \widehat{v_n}^{\pm}(y) &= C_n^{\pm} e^{\mp\theta y} \pm \tfrac{2\pi\wp}{\lambda+in} A_n^{\pm} e^{\mp(2\pi\wp)y}, \end{aligned} \tag{3.15}$$

where $B_n^{\pm}$ and $C_n^{\pm}$ are constants and we introduce a new parameter θ, given by $\theta^2 := (2\pi\wp)^2 + \frac{\lambda+in}{\nu}$. At present, we make the assumption that $(\lambda + in) \neq 0$, and consider the special case $(\lambda + in) = 0$ later on.

We next deal with the evolution equations of the immersed fiber (3.7) in the same way, by using the transformations (3.11) and solutions (3.14)-(3.15). Without introducing any additional unknowns, the Fourier coefficients for the fiber position are given by

$$\begin{aligned} \widehat{\xi_n} &= \tfrac{1}{\lambda+in} B_n^{+} - \tfrac{i2\pi\wp}{(\lambda+in)^2} A_n^{+}, \\ \widehat{\eta_n} &= \tfrac{1}{\lambda+in} C_n^{+} + \tfrac{2\pi\wp}{(\lambda+in)^2} A_n^{+}. \end{aligned} \tag{3.16}$$

The superscripts "$\pm$" refer to the solutions on the separate domains $\Omega^{\pm}$, which are determined by the two sets of unknowns $\{A_n, B_n, C_n\}^{(\pm)}$ respectively. There remains the question of which set of unknowns we should use to express the positions $\widehat{\xi_n}$ and $\widehat{\eta_n}$ at the immersed interface. Indeed, the particular choice is somewhat arbitrary and either "+" or "−" coefficients can be used to express $\widehat{\xi_n}$ and $\widehat{\eta_n}$ in (3.16), owing to the incompressibility conditions we will derive in the next section. We therefore chose the "+" coefficients here, and will address this issue further in the next section.

3.3 Linear system

Once the constants $A_n^{\pm}$, $B_n^{\pm}$, $C_n^{\pm}$ are determined, the solutions of the linearized IB system will be given explicitly, based on the expressions of Fourier coefficients (3.14)-(3.16) and

transformations (3.11). In order to determine the six unknowns of each wave mode, we need to derive a linear system of six equations relating the coefficients. Four of the equations are obtained from the jump conditions (3.4)-(3.6) and the remaining two come from the incompressibility condition (3.10) applied on either side of the fiber. Furthermore, if we notice that our efforts focus on the motion of the fiber, a simpler system can derived ultimately, which is made up of two equations that involve only the unknowns $\widehat{\xi_n}$ and $\widehat{\eta_n}$. This system can be viewed as an eigenvalue problem where the vector of fiber Fourier coefficients represents an eigenvector, and the forcing amplitude ϵ is the corresponding eigenvalue.

In the end, numerical methods are applied to calculate the eigenvalues of the system, from which we can predict the unstable regions in parametric plane; that is, the fiber is excited to produce resonance rather than decaying in time. Depending on the values $(\lambda + in)$ being trivial or not, the character of solutions displays differently. Hence, we will consider these two cases separately.

3.3.1 Case $(\lambda + in) \neq 0$

By substituting the coefficients of fluid velocity (3.15) into the transformed incompressibility (3.12) on both sides of the fiber, we get the first two equations of the linear system

$$\begin{aligned} i2\pi\wp B_n^+ - \theta C_n^+ &= 0, \\ i2\pi\wp B_n^- + \theta C_n^- &= 0. \end{aligned} \tag{3.17}$$

The continuous jump conditions for the fluid velocity (3.6) result in another two equations

$$\begin{aligned} B_n^+ - \tfrac{i2\pi\wp}{\lambda+in} A_n^+ - B_n^- + \tfrac{i2\pi\wp}{\lambda+in} A_n^- &= 0, \\ C_n^+ + \tfrac{2\pi\wp}{\lambda+in} A_n^+ - C_n^- + \tfrac{2\pi\wp}{\lambda+in} A_n^- &= 0. \end{aligned} \tag{3.18}$$

On looking at these last two equations, it is clear why the "+" coefficients $\{A_n^+, B_n^+, C_n^+\}$ in (3.16) can be replaced by those "−" coefficients without any contradiction. The continuity conditions of velocity (3.6) facilitate the symmetric proposition of two groups of unknowns in (3.18), which validates the equivalence discussion after (3.16) in the end of previous section.

There remain another two jump conditions, (3.4) and (3.5), which give rise to the last

two equations for the linear system

$$
\begin{array}{lllllllll}
0= & \left(\sigma\epsilon\frac{(2\pi\wp)^2}{\lambda+i(n-1)}\right) & \{ & i & B^+_{n-1} & + & \frac{2\pi\wp}{\lambda+i(n-1)} & A^+_{n-1} & \} \\
+ & & \{ & (-\nu\theta-\sigma\frac{(2\pi\wp)^2}{\lambda+in}) & B^+_n & + & (\nu\frac{i(2\pi\wp)^2}{\lambda+in}+\sigma\frac{i(2\pi\wp)^3}{(\lambda+in)^2}) & A^+_n & \\
 & & & -\nu\theta & B^-_n & + & \nu\frac{i(2\pi\wp)^2}{\lambda+in} & A^-_n & \} \\
- & \left(\sigma\epsilon\frac{(2\pi\wp)^2}{\lambda+i(n+1)}\right) & \{ & i & B^+_{n+1} & + & \frac{2\pi\wp}{\lambda+i(n+1)} & A^+_{n+1} & \},
\end{array}
$$

$$
\begin{array}{lllllllll}
0= & \left(\sigma\epsilon\frac{(2\pi\wp)^2}{\lambda+i(n-1)}\right) & \{ & i & C^+_{n-1} & + & \frac{i2\pi\wp}{\lambda+i(n-1)} & A^+_{n-1} & \} \\
+ & & \{ & -\sigma\frac{(2\pi\wp)^2}{\lambda+in} & C^+_n & + & (-1-\sigma\frac{(2\pi\wp)^3}{(\lambda+in)^2}) & A^+_n & \\
 & & & 0 & C^-_n & + & 1 & A^-_n & \} \\
- & \left(\sigma\epsilon\frac{(2\pi\wp)^2}{\lambda+i(n+1)}\right) & \{ & i & C^+_{n+1} & + & \frac{i2\pi\wp}{\lambda+i(n+1)} & A^+_{n+1} & \}.
\end{array}
\tag{3.19}
$$

Equations (3.19) appear complicated compared with the earlier equations, partly because they don't simply relate coefficients with indices "n", but rather couple them together the adjacent modes having indices "$n+1$" and "$n-1$". The reason for wave modes in (3.19) drifting left and right is owing to time dependence of the stiffness $\kappa(t)$ in (3.3). When we apply the Fourier transformation (3.11) to the jump condition (3.4) or (3.5), its left hand side involves a multiplication of the stiffness, $\kappa(t)$, which employs the time-dependent form (3.3) and modulates the current time mode e^{int} to another two adjacent ones $e^{i(n+1)t}$ and $e^{i(n-1)t}$. The coupled time modes introduce various fiber coefficients as $\{A_{n(\pm1)}, B_{n(\pm1)}, C_{n(\pm1)}\}$ in (3.19). This is also the main difference between present work with the publication [38], where Stockie and Wetton studied the model of unforced fiber. In their model, constant stiffness leaded to an homogenous system, which depended on the n-th modes only. Hence, their system was well-determinant and asymptotic expansions could be derived for the decay rates and frequencies explicitly.

Notice at this point that for each n, we have six equations in (3.17), (3.18) and (3.19). These six equations relate together the six unknown coefficients, $A^\pm_n$, $B^\pm_n$, and $C^\pm_n$, with the neighboring coefficients (having indices $n+1$ and $n-1$), and so we now have sufficient equations to close the system. However, it is still not possible to solve this system because it is infinite-dimensional, and so our approach is to truncate at some finite value $|n| \leq N$, and then calculate the eigenvalues of the system approximately. This approximation makes sense if we assume that the coefficients tend to zero in magnitude for large $|n|$; this is a claim that we cannot verify *a priori*, but which we will investigate later on when we actually

compute the eigenvalues.

We will now reduce the resulting system into one involving the coefficients $\widehat{\xi_n}$ and $\widehat{\eta_n}$ only, which we will see it later eases the computation of eigenvalues tremendously. For this purpose, we express the unknowns $A_n^{\pm}$, $B_n^{\pm}$, $C_n^{\pm}$ in terms of the fiber Fourier coefficients $\widehat{\xi_n}$ and $\widehat{\eta_n}$ in turn. This can be realized, by combining the equations of the system (3.17), (3.18) with the fiber solutions (3.16) and noticing that wave modes of single index n are involved in these equations, and finally, we get

$$\begin{aligned} A_n^+ &= (\lambda+in)^2\left(\tfrac{\theta}{\theta-\wp}\right)\left[\tfrac{\widehat{\eta_n}}{\wp}-i\tfrac{\widehat{\xi_n}}{\theta}\right], & A_n^- &= (\lambda+in)^2\left(\tfrac{-\theta}{\theta-\wp}\right)\left[\tfrac{\widehat{\eta_n}}{\wp}+i\tfrac{\widehat{\xi_n}}{\theta}\right], \\ B_n^+ &= (\lambda+in)\left(\tfrac{i\theta}{\theta-\wp}\right)\left[\widehat{\eta_n}-i\widehat{\xi_n}\right], & B_n^- &= (\lambda+in)\left(\tfrac{-i\theta}{\theta-\wp}\right)\left[\widehat{\eta_n}+i\widehat{\xi_n}\right], \\ C_n^+ &= (\lambda+in)\left(\tfrac{-\wp}{\theta-\wp}\right)\left[\widehat{\eta_n}-i\widehat{\xi_n}\right], & C_n^- &= (\lambda+in)\left(\tfrac{-\wp}{\theta-\wp}\right)\left[\widehat{\eta_n}+i\widehat{\xi_n}\right]. \end{aligned} \tag{3.20}$$

Now, since we have assumed that $(\lambda+in)\neq 0$, by substituting the expressions (3.20) into equations (3.19), we obtain the final simplified system as

$$\left\{2\left(\frac{\nu}{\sigma}\right)(\lambda+in)(\theta+2\pi\wp)\frac{1}{(2\pi\wp)^2}+1\right\}\widehat{\xi_n}+i\epsilon(\widehat{\xi_{n+1}}-\widehat{\xi_{n-1}}) = 0, \tag{3.21}$$

$$\left\{2\left(\frac{\nu}{\sigma}\right)(\lambda+in)(\theta+2\pi\wp)\frac{\theta}{(2\pi\wp)^3}+1\right\}\widehat{\eta_n}+i\epsilon(\widehat{\eta_{n+1}}-\widehat{\eta_{n-1}}) = 0. \tag{3.22}$$

These expressions contain all the information we need about the relationship of the Fourier coefficients to analyze the stability of the immersed boundary problem.

3.3.2 Case $(\lambda+in)=0$

This case only occurs when both $n=0$ and $\lambda=0$, and it corresponds to the trivial solutions for u,v,p, which imply the Fourier coefficients to be zero in expressions (3.14) and (3.15). This case needs to be considered separately because some constraint conditions are automatically satisfied, such as the velocity continuity (3.6) conditions and incompressibility (3.10). The remaining two jump conditions in terms of the fiber coefficients ξ and η in (3.4) and (3.5) are significantly simplified and rewritten as

$$\widehat{\xi_0}+i\epsilon(\widehat{\xi_1}-\widehat{\xi_{-1}}) = 0, \tag{3.23}$$

$$\widehat{\eta_0}+i\epsilon(\widehat{\eta_1}-\widehat{\eta_{-1}}) = 0. \tag{3.24}$$

Notice, that these two equations also follow from the expressions in the case $(\lambda+in)\neq 0$ if we set $\lambda=0$ and $n=0$ in (3.21) and (3.22).

3.4 Floquet analysis

3.4.1 Truncated linear system

In previous sections, we obtain the linear system that describes the evolution of the immersed boundary in terms of the Fourier coefficients. Now we will perform the stability analysis for equations (3.21)-(3.24) using the techniques of Floquet theory.

The equations (3.21)-(3.22), which couple multiple Fourier coefficients, are derived from the jump conditions for the pressure (3.22) and the tangential component of the normal velocity derivative (3.21). In general, each of the coefficients $\widehat{\xi_n}$ and $\widehat{\eta_n}$ can be complex valued. By taking $\widehat{\xi_n} = \widehat{\xi_n^r} + i\widehat{\xi_n^i}$, the equation (3.21) becomes

$$(\phi_n^r + i\phi_n^i)(\widehat{\xi_n^r} + i\widehat{\xi_n^i}) + i\epsilon(\widehat{\xi_{n+1}^r} + i\widehat{\xi_{n+1}^i} - \widehat{\xi_{n-1}^r} - i\widehat{\xi_{n-1}^i}),$$

where we have used $\phi_n := \phi_n^r + i\phi_n^i$ to denote the complex form of the coefficients $\{2\left(\frac{\nu}{\sigma}\right)(\lambda + in)(\theta + 2\pi\wp)\frac{1}{(2\pi\wp)^2} + 1\}$ in (3.21). By setting the real and imaginary parts equal to zero separately, we have

$$\begin{cases} Re: & (\phi_n^r\widehat{\xi_n^r} - \phi_n^i\widehat{\xi_n^i}) - \epsilon(\widehat{\xi_{n+1}^i} - \widehat{\xi_{n-1}^i}) = 0, \\ Im: & (\phi_n^i\widehat{\xi_n^r} + \phi_n^r\widehat{\xi_n^i}) + \epsilon(\widehat{\xi_{n+1}^r} - \widehat{\xi_{n-1}^r}) = 0. \end{cases} \tag{3.25}$$

In addition to these equations, a similar treatment of (3.22) leads to the additional two equations

$$\begin{cases} Re: & (\psi_n^r\widehat{\eta_n^r} - \psi_n^i\widehat{\eta_n^i}) - \epsilon(\widehat{\eta_{n+1}^i} - \widehat{\eta_{n-1}^i}) = 0, \\ Im: & (\psi_n^i\widehat{\eta_n^r} + \psi_n^r\widehat{\eta_n^i}) + \epsilon(\widehat{\eta_{n+1}^r} - \widehat{\eta_{n-1}^r}) = 0, \end{cases} \tag{3.26}$$

by setting $\widehat{\eta_n} = \widehat{\eta_n^r} + i\widehat{\eta_n^i}$ and the coefficients $\left\{2\left(\frac{\nu}{\sigma}\right)(\lambda + in)(\theta + 2\pi\wp)\frac{\theta}{(2\pi\wp)^3} + 1\right\}$ to its complex form $\psi_n := \psi_n^r + i\psi_n^i$ in the equation (3.22).

Now combining all four equations together, we can build up a linear system by defining the vector $v = (\cdots, v_{-N}, \cdots, v_{-1}, v_0, v_1, \cdots, v_N, \cdots)^T$ with an infinite number of entries. Each v_n has 4 components and is denoted by $v_n = [Re(\widehat{\xi_n}), Im(\widehat{\xi_n}), Re(\widehat{\eta_n}), Im(\widehat{\eta_n})]^T$. In general, it is plausible for us to truncate the infinite system at some finite number N, say $-N \leq n \leq N$, because it turns out in practice that the magnitudes of Fourier coefficients decrease as the index $|n|$ increases (which will be checked later on). The truncated linear system may now be written:

$$v^T\,[\mathcal{A}(\epsilon)]_{4(2N+1)\times 4(2N+1)} = 0. \tag{3.27}$$

3.4.2 Derivation of eigenvalue problem

The expression $e^{\lambda t} = e^{(\alpha+i\beta)t}$ in (3.11) is usually referred to as the Floquet multiplier. The standard approach to analyzing stability is to determine the marginal stability boundaries corresponding to $\alpha = 0$, for which the Floquet multipliers are $e^{\lambda t} = e^{i\beta t}$. These stability boundaries decompose the parameter space into regions where the solution is stable ($\alpha < 0$) and those where it is unstable ($\alpha > 0$). These results will be of great benefit to us in predicting the behavior of immersed fibers under the influence of periodic variations in the stiffness parameter.

We focus on the marginal boundaries at $\alpha = 0$, for which the modes $e^{(\lambda+in)t} = e^{i(\beta+n)t}$ whose values must be either real or occurrent in complex-conjugate pairs. Furthermore, β can be restricted to the interval $[0, \frac{1}{2}]$ as we will describe next. We rewrite the modes as $e^{i(\beta+n)t} = e^{i2\pi(\beta+n)(t/2\pi)} := e^{i2\pi(\beta+n)}$, where time t can be considered modulo 2π because the internal forcing through the dimensionless stiffness in (2.15) is a 2π- periodic function of time. Meanwhile, we can restrict ourselves to the range $0 \leq \beta \leq \frac{1}{2}$ only for two reasons. First of all, β is modulo 1 in $e^{i2\pi(\beta+n)}$, otherwise, any integer multiples greater than one will be absorbed into n; moreover, the modes for $\frac{1}{2} < \beta < 1$ have a complex-conjugate that corresponds to a β in the range $0 < \beta < \frac{1}{2}$. As a result, all $\beta \neq 0$ or $\frac{1}{2}$ can be disregarded because they lead to values of $e^{(\lambda+in)t}$ with non-zero real part of complex number λ. They are of no interest in determining the stability boundaries. From the definition $e^{i2\pi(\beta+n)}$, we list all possible cases easily. Every real Floquet multipliers correspond to two situations: positive number with $\beta = 0$, called *harmonic case* ; negative one with $\beta = \frac{1}{2}$, called *subharmonic case* .

We observe here that the solution to (3.21)–(3.24) (or the truncated system (3.27)) could very well be complex, although physically, only real values of the fiber positions $\xi(s,t)$ and $\eta(s,t)$ make physical sense. Consequently, we must impose "reality conditions" on the Fourier coefficients $\widehat{\xi_n}$ and $\widehat{\eta_n}$. Following [17], we specify the following conditions:

- Harmonic Case ($\beta = 0$): $\widehat{\xi_{-n}} = \widehat{\xi_n}^*$, $\widehat{\eta_{-n}} = \widehat{\eta_n}^*$;
- Subharmonic Case ($\beta = \frac{1}{2}$): $\widehat{\xi_{-n}} = \widehat{\xi_{n-1}}^*$, $\widehat{\eta_{-n}} = \widehat{\eta_{n-1}}^*$,

where a superscript "*" refers to the complex conjugate.

By applying these reality conditions, the expressions for all unknowns (3.11) can be rewritten in terms of the non-negative Fourier coefficients (for $n \geq 0$). Consequently, the

truncated linear system (3.27) is reduced to a problem of size $4(N+1) \times 4(N+1)$. The reality conditions correspond to a lower boundary condition with $\widehat{\xi_{-1}} = \widehat{\xi_1}^*$ for the harmonic case, or $\widehat{\xi_{-1}} = \widehat{\xi_0}^*$ for the subharmonic case (and similarly for the $\widehat{\eta}$ variable).

Finally, we come to the stage of constructing an eigenvalue problem from the forgoing equations. The matrix $\mathcal{A}(\epsilon)$ in (3.27) is linear in ϵ, and so can be written as $\mathcal{A}(\epsilon) = \mathbf{D} + \epsilon\mathcal{C}$, where $\mathbf{D}$ and $\mathbf{C}$ are $(4N+4) \times (4N+4)$ matrices. This is more naturally written in the form

$$-\left(\mathcal{D}^{-1}\mathcal{C}\right)\, v = \frac{1}{\epsilon}\, v, \tag{3.28}$$

wherein it is clear that $\frac{1}{\epsilon}$ can be considered as an eigenvalue, and v the eigenvector.

3.5 Analytic results

In this section, we study the stability of the flat immersed fiber by investigating the eigenvalue plots obtained from the problem (3.28), and discuss the influence on these figures by varying the system parameters. To compute the solution to the eigenvalue problem, we select values of the parameters ν and σ and then vary the wavenumber $\wp$, determining a sequence of eigenvalues $1/\epsilon$ corresponding to each wavenumber $\wp$. Only real values of ϵ have any physical interest, and so we select the largest real eigenvalue $1/\epsilon$ in the problem (3.28), which corresponds to the smallest positive amplitude ϵ. By plotting these eigenvalues as points $(\wp, \epsilon)$, we can then trace out the boundaries of the stability region in parameter space. We maintain the separation between harmonic and subharmonic solution modes, and note also that it is sufficient to truncate the series solution at $N = 60$ terms, for which the magnitude of the neglected coefficients is sufficiently small.

As shown in Fig. 3.1 for the fixed values of $\nu = 1.5e-4$ and $\sigma = 5e-6$, the blue dots represent the eigenvalues of the harmonic modes, and the red dots are those of the subharmonic modes. The corresponding marginal stability boundaries are traced out by the colored lines composed of these eigenvalues for both cases. The areas enclosed above and inside the marginal stability boundaries represent regions of instability, and are also known as "fingers" or "tongues" because of their characteristic shape. We see that there are multiple, non-overlapping tongues moving out to the right as $\wp$ increases, which alternate between harmonic and subharmonic modes.

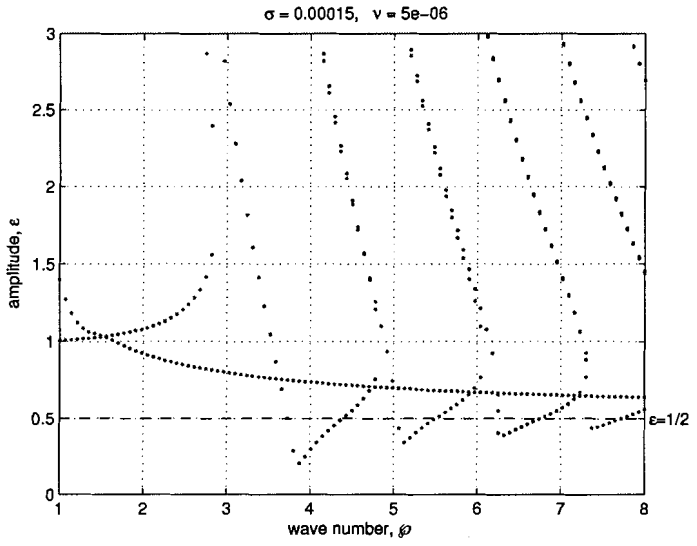

Figure 3.1: Stability diagrams, depicting the fiber amplitude ϵ as a function of wavenumber $\wp$, for holding parameters σ and ν defined in (2.16). The marginal stability boundaries are traced out by individual eigenvalues. The red points correspond to the harmonic modes and the blue ones to subharmonic modes. A zoomed-in view of the regions of instability is given in Fig. 3.2.

It is essential to keep in mind that instability (i.e., resonance) can only occur within the portion of the tongue lying below the line $\epsilon = \frac{1}{2}$, which corresponds to the fiber stiffness being positive in (2.6) for any value of t. Fig. 3.2 enlarges the first two regions of instability for a selected harmonic mode (at $\wp = 4$) and successively a subharmonic one (around $\wp = 5.2$), which is obtained by zooming in the Fig. 3.1 and based on the same parameters as before.

Another restriction on parameters is that we can only consider those tongues of instability that impinge on integer values of $\wp$, since only integer wavenumbers make any physical sense in our situation. In the eigenvalue plot given in Fig. 3.1, we see that only the first tongue represents a physical instability, corresponding to a harmonic mode with wavenumber $\wp = 4$; all other tongues "touch down" at non-integer wavenumbers. These results are quite similar qualitatively to those reported in [8] for a circular immersed boundary. However, our analysis leads to a much simpler linear system (3.21)–(3.24) that avoids the presence of complex Bessel functions.

Next, we consider the effect on the shape and location of the tongues by varying the values of parameters in the system. When we adjust the parameters σ (stiffness κ_c) or ν (viscosity μ), the tongues move in a predictable fashion, as indicated in Fig. 3.2. For example, as ν decreases, the tongues will move downward; on the other hand, the tongues shift horizontally in response to variations in stiffness σ.

In order to demonstrate that changes in parameter values yield results that are consistent over all eigenvalue plots, another two examples will be considered here, that will be used to describe the effect of parameter changes to the stability diagram. These results will also be compared with numerical results computed in Chapter 5. Fig. 3.3 depicts the stability diagram for $\sigma = 9.9e-4$ and $\nu = 2.2e-4$ (which we refer to as "*case II*"), where we see that the first (and only) unstable mode is $\wp = 2$. Fig. 3.4 is generated for $\sigma = 1.8e-4$ and $\nu = 9.8e-5$, and illustrates the situation where the $\wp = 4$ mode is unstable (we call this one "*case IV*").

At first, we consider the impact of changing stiffness on the position of the tongues. As depicted in Fig. 3.2, we know that

- when stiffness κ_c (or σ) is increased, the fingers will move towards the left, and vice versa.

Fig. 3.5 shows more clearly the influence of the changes in the stiffness parameter. As κ_c

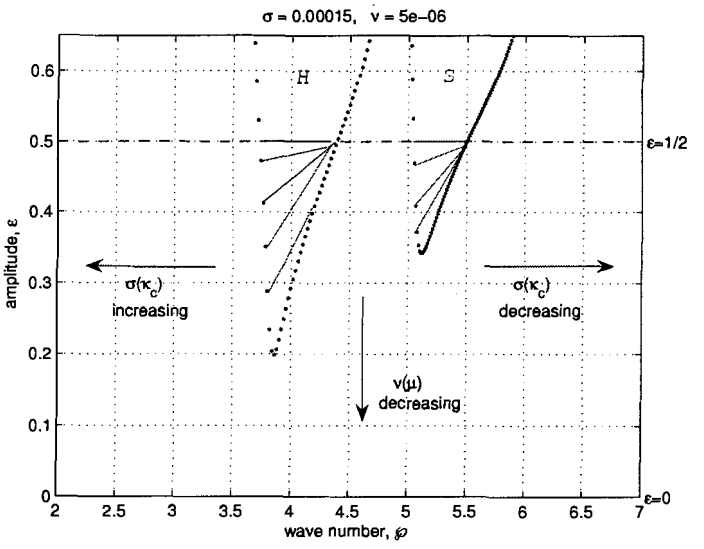

Figure 3.2: Stability diagram obtained by zooming in on Fig. 3.1 near the first two unstable modes in respect to a Harmonic (H) and Subharmonic (S) case. The shaded areas correspond to the instability in the parametric plane. The shift in location of tongues in response to changes in parameters $\sigma(\kappa_c)$ and $\nu(\mu)$ is also indicated.

is increased from 10000 to 40000, the unstable tongue moves towards left. There is initially no physical instability, until κ_c increases above 20000, at which point the $\wp = 2$ mode becomes unstable. As κ_c increases beyond 30000, the $\wp = 2$ mode stabilizes and resonance no longer occurs. At the same time, as the tongues move to the left, they also migrate slightly downward. This behavior is due to a destabilizing effect of increasing stiffness. Now the internal forces are being faded out gradually and the system is dominated by the effect of viscous damping, so that every physical wave modes of instability are stabilized in the parametric plane.

Secondly, we investigate the effect of changes in the viscosity on the vertical motion of the tongues, and we have that

- when viscosity μ (or ν) is increased, the fingers will move upwards vertically, owing to the stabilizing effect of viscous forces.

As a tongue moves vertically upward, the result is to shrink the region of instability so that some unstable modes no longer lead to parametric resonance at a given amplitude of oscillation ϵ. Therefore, the minimum forcing amplitude ϵ required to excite an instability

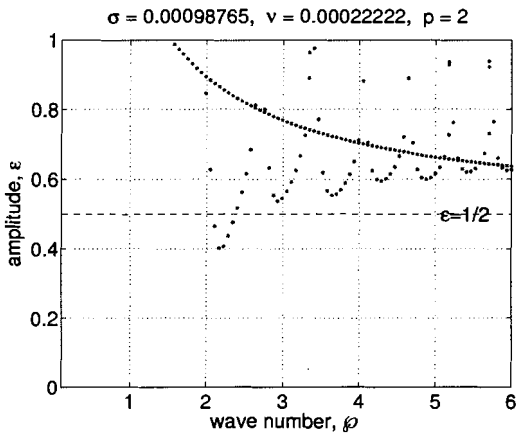

$\kappa_c = 20000$

Figure 3.3: Case II: stability diagram of the first unstable mode $\wp = 2$ occurring for $\sigma = 9.9e-4$ and $\nu = 2.2e-4$, which will be used to show the impact of the changes in the *stiffness* on the stability boundaries. The analytic results are shown in Fig. 3.5, and numerical comparisons are displayed in Fig. 5.13.

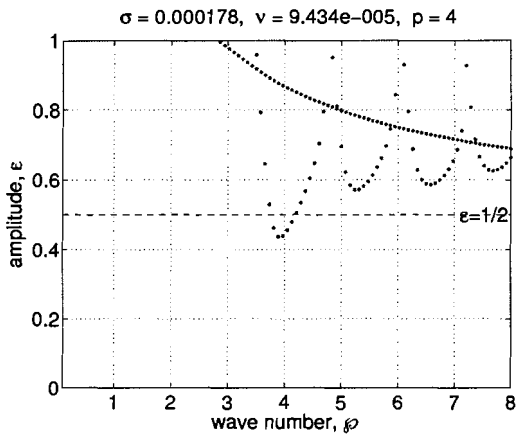

$\mu = 1.0$

Figure 3.4: Case IV: stability diagram of the first unstable mode $\wp = 4$ occurring for $\sigma = 1.8e-4$ and $\nu = 9.8e-5$, which will be used to show the impact of the changes in the *viscosity* to the stability boundaries. The analytic results are shown in Fig. 3.6, and numerical comparisons are displayed in Fig. 5.14.

is increased. If the viscosity is increased further, the bottom of the tongue may move above the line $\epsilon = \frac{1}{2}$, at which point resonance is no longer possible.

On the other hand, if ν is decreased, the tongues will move downward vertically as depicted in Fig. 3.2. In the inviscid limit, as $\nu \to 0$, each tongue extends downward to touch the horizontal axis, $\epsilon = 0$, at a single point. Each of these points corresponds to a natural resonance in the unforced ($\epsilon = 0$ in (2.6)) system. An example will be presented in Section 5.3, indicating the behavior of the damped oscillations in an unforced fiber as viscosity goes to zero. Fig. 3.6 illustrates the effect on the unstable tongues of varying the viscosity $\mu = 0.5,\ 1.0,\ 2.0,\ 3.0$ for the given value of $\sigma = 1.8e-4$.

This concludes the analytical part of this thesis. The previous two examples will be computed in Chapter 5 to compare with the analytic results. But first, the next chapter describes the implementation of the IB method used to compute the numerical results.

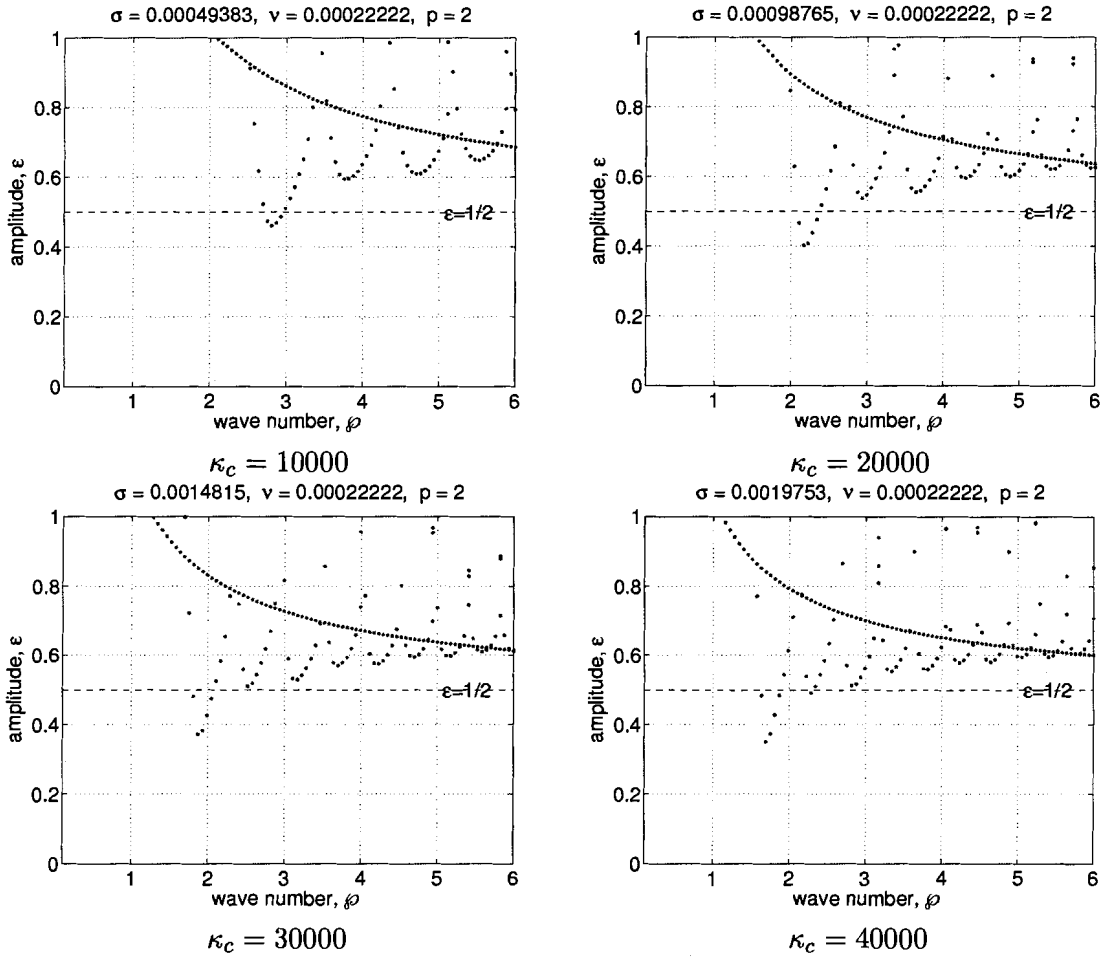

Figure 3.5: A series of plots showing the impact of the changes in *stiffness* on the movement of stability boundaries in parametric space. The viscosity parameter is fixed at $\nu = 2.2e-4$, and four different stiffness parameters are selected: $\sigma = 4.9e-4,\ 9.8e-4,\ 1.5e-3,\ 2.0e-3$.

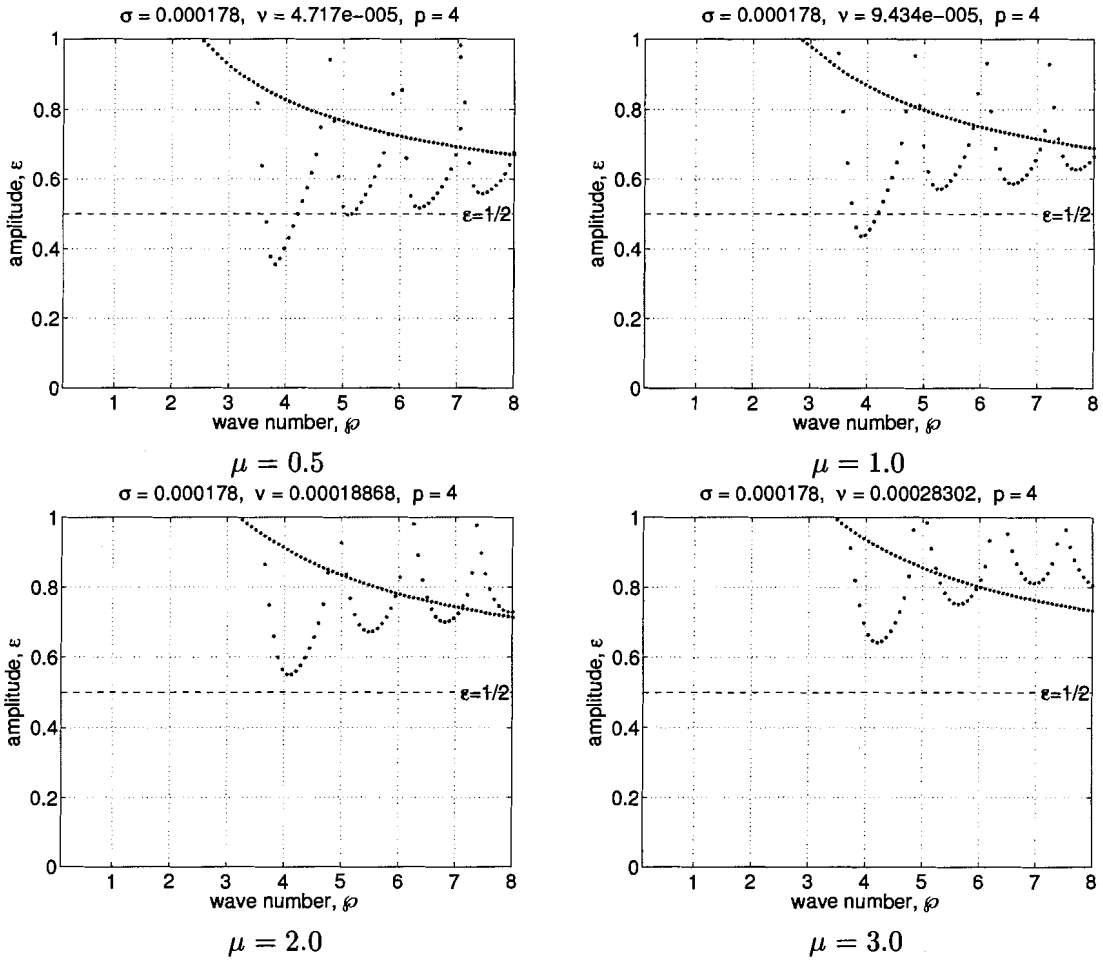

Figure 3.6: A series of plots showing the impact of the changes in *viscosity* on the location of stability boundaries in the parameter plane. For fixed stiffness parameter $\sigma = 1.8e-4$ and four different viscosity parameters $\nu = 4.7e-5,\ 9.4e-5,\ 1.9e-4,\ 2.8e-4$.

Chapter 4

Computational Method

In this chapter, we describe the Immersed Boundary (IB) method for simulating the interaction between an incompressible fluid and an immersed boundary. This method was originally developed by C.S. Peskin in [26, 27, 29]. Nonetheless, many later works improved on the original scheme, such as the IB method with higher-order accuracy [12] and the Immersed Interface method [21]. In the present thesis, we will employ the IB method as originally formulated in [26], and incorporate with a fast Poisson solver.

Instead of discretizing the non-dimensionalized equations, we will start from the dimensional IB equations (2.1)-(2.9) in Section 2.1, which will make it easier for us to compare with published results in cgs units [7, 22, 19, 8]. The computational domain is a square box that is exactly equal to the physical domain in both x- and y-directions, as defined in Section 2.1. Periodic boundary conditions are applied in both directions. Both fluid and fiber are initially taken to be at rest. Only a small perturbation is imposed on the initial position of the immersed fiber, with the maximum amplitude $a \approx O(L/20)$ measuring the distance that the fiber is away from its equilibrium state. Since the amplitude of the oscillations is much smaller than the extent of computational domain in the y-direction, we assume that the motion of the fiber does not interfere significantly with the fluid at the vertical boundaries (which justifies our use of periodic boundary conditions in y).

As mentioned in the Introduction, the incompressible viscous Navier-Stokes equations are discretized on a fixed uniform Eulerian lattice while the fiber evolution is described by a moving Lagrangian array of points. Both sets of points do not necessarily coincide during the computation, and information is communicated between them through the assistance of smooth approximations to the Dirac delta function.

This chapter is organized as follows. In the first section, we review a projection method for solving the incompressible Navier-Stokes equations with general external forces. After reviewing the fluid solver, we present the aspects of the numerical discretization that pertain to the evolution of the fiber and the computation of the force exerted by the fiber on fluid. Numerical simulations demonstrating the stability and convergence of the method will be discussed in the following chapter.

4.1 Fluid component

A wide array of numerical schemes have been proposed for solving the viscous incompressible Navier-Stokes equations. One especially popular approach is called the *fractional step method* that was introduced by Chorin in [5, 6] and was followed by many other variants in the literature [1, 4, 25]. These methods are also collectively known as *projection methods*, since they are based on computing an intermediate velocity independent of the divergence-free constraint, and then projecting the velocity onto the subspace of divergence-free vector fields. In this section, we discuss a particular version of the general projection method proposed by Chorin.

4.1.1 Projection method

In the method proposed in the initial paper of Chorin, the first fractional step involved computing the fluid velocity by ignoring the incompressibility constraint and updating the velocity using the viscous and convective terms in the Navier Stokes equations. The particular update proposed applied the velocity updates in each coordinate direction independent, using alternative direction approach. In the second step, a Poisson equation was solved that serves to project the velocity onto the divergence-free subspace.

The projection step can be written generally in terms of a projection operator P, which projects an arbitrary vector field onto the divergence-free subspace. With the use of the mapping P, we can then eliminate the continuity constraint $\nabla \cdot \mathbf{u} = 0$ and the pressure variable $p(\mathbf{x}, t)$ from the Navier-Stokes equations. Here, we follow the notation of Peskin in [26] and define the projection operator P as follows

$$\mathbf{w}^D = P\mathbf{w}, \tag{4.1}$$

such that

$$\nabla \cdot \mathbf{w}^D = 0 \qquad \text{and} \qquad \mathbf{w} = \mathbf{w}^D + \nabla\psi, \tag{4.2}$$

where ψ is a scalar, $\mathbf{w}$ and $\mathbf{w}^D$ are vectors, and $\mathbf{w}^D$ is divergence-free. From the definition, it is easy to verify the following properties:

(1) P is linear.

(2) For any scalar ψ, $P\nabla\psi = 0$.

(3) For any vector $\mathbf{w}^D$ such that $\nabla \cdot \mathbf{w}^D = 0$, we also have $P\mathbf{w}^D = \mathbf{w}^D$.

These properties will be used later on.

With respect to the fluid equations, we consider the constant-density viscous incompressible Navier-Stokes (2.1)-(2.2), together with periodic boundary conditions on a square domain Ω. By applying projection operator P to both sides of the momentum equations (with divergence-free velocity denoted $\mathbf{u}^D$), we find that

$$\rho\left(\mathbf{u}_t^D + \mathbf{u}^D \cdot \nabla\mathbf{u}^D\right) = \mu\triangle\mathbf{u}^D + \mathbf{f}^D. \tag{4.3}$$

In equation (4.3), the incompressibility condition (2.2) is satisfied automatically, owing to the action of the projection P, as long as we also project the force density $\mathbf{f}$ onto its divergence-free image $\mathbf{f}^D$ in (4.3); in other words, $\mathbf{f}^D = P\mathbf{f}$.

An alternative way to formulate the project method, based on the definition of the project operator, leads to a simple update scheme for the velocity. From the definition (4.1)–(4.2), we can introduce a scalar field, ψ, that is used to update the intermediate velocity to make it divergence free. The projection method can then be written as the following three-step scheme:

$$\text{Step 1.} \quad \text{Solving } \mathbf{u} \text{ from} \quad \rho\left(\mathbf{u}_t + \mathbf{u} \cdot \nabla\mathbf{u}\right) = \mu\triangle\mathbf{u} + \mathbf{f}; \tag{4.4}$$

$$\text{Step 2.} \quad \text{Solving } \psi \text{ from} \quad \triangle\psi = \nabla \cdot \mathbf{u}; \tag{4.5}$$

$$\text{Step 3.} \quad \text{Solving } \mathbf{u}^D \text{ from} \quad \mathbf{u}^D = \mathbf{u} - \nabla\psi. \tag{4.6}$$

The resulting velocity, $\mathbf{u}^D$, satisfies the incompressible Navier-Stokes equations. We will show in the next section how the projection method can be discretized explicitly in time so that a Fast Fourier Transform (FFT) can be used to solve the Poisson equation (4.5), since the domain is rectangular and the coefficients (density and viscosity) are constant. As a result, this scheme can be very efficient.

4.1.2 Numerical scheme

Because we have assumed in Section 2.1 that the domain is rectangular, the problem can be discretized on a square lattice having $h = \Delta x = \Delta y$ as the mesh width. The mesh points are denoted as $\mathbf{x}_{ij} = (x_i, y_j) = (ih, jh)$ for $0 \leq i, j \leq N-1$. A similar notation can be extended to all fluid variables defined on $\Omega(x, y)$, such as $\mathbf{u}_{ij} = \mathbf{u}(\mathbf{x}_{ij}, t)$ and $\mathbf{f}_{ij} = \mathbf{f}(\mathbf{x}_{ij}, t)$.

Let Δt be the length of the time step and n be the index of time step, hence we have $\mathbf{u}^n = \mathbf{u}(\mathbf{x}, n\Delta t)$, $\mathbf{f}^n = \mathbf{f}(\mathbf{x}, n\Delta t)$. Now, supposing that we already have available to us the updated force values, $\mathbf{f}^{n+1}(\mathbf{x})$, we can present the discrete form of the projection method for the Navier-Stokes equations. First, define the difference operators D_k^0, D_k^+, D_k^- $(k = x, y)$ for the first-order derivatives as follows:

$$\begin{aligned}
(D_k^0\varphi)(\mathbf{x}) &= \frac{\varphi(\mathbf{x} + h\mathbf{e}_k) - \varphi(\mathbf{x} - h\mathbf{e}_k)}{2h}; \\
(D_k^+\varphi)(\mathbf{x}) &= \frac{\varphi(\mathbf{x} + h\mathbf{e}_k) - \varphi(\mathbf{x})}{h}; \\
(D_k^-\varphi)(\mathbf{x}) &= \frac{\varphi(\mathbf{x}) - \varphi(\mathbf{x} - h\mathbf{e}_k)}{h};
\end{aligned}$$

where $\{\mathbf{e}_k\}$ $(k = x, y)$ is the standard basis for $\Re^2$. We can then define additional difference operators such as $D_k^+ D_k^-$, the central difference approximation to the second order derivative in each direction; $\mathbf{D}^0 = (D_x^0, D_y^0)^T$, which is the central difference approximation to the gradient operator ∇; $\mathbf{D}^{\pm}$, corresponding to forward and backward approximations of the gradient; and $\mathbf{D}^+ \cdot \mathbf{D}^-$, a five point difference approximation to the Laplacian operator $\triangle$. Now, for example, we can use the notation $\mathbf{D}^0 \cdot \mathbf{u}$ to represent a second order centered difference approximation to the divergence of the vector field $\mathbf{u}$.

Using these definitions, we may now write the fractional-step discretization of the projection method in (4.4)-(4.6). The first step is to calculate an intermediate velocity field $\mathbf{u}^{**}$, which is not divergence free and comes from solving the following difference equations:

$$\left[I + \Delta t \left(u^n D_x^0 - (\frac{\mu}{\rho}) D_x^+ D_x^- \right) \right] \mathbf{u}^* = \mathbf{u}^n + \Delta t (\frac{\mathbf{f}^{n+1}}{\rho}); \tag{4.7}$$

$$\left[I + \Delta t \left(v^n D_y^0 - (\frac{\mu}{\rho}) D_y^+ D_y^- \right) \right] \mathbf{u}^{**} = \mathbf{u}^*. \tag{4.8}$$

These equations represent the alternative direction implicit discretization of the convective and viscous terms, which are applied separately in the x- and y-directions. By substituting (4.8) into (4.7), and ignoring terms of order $(\Delta t)^2$, the resulting discretizing scheme is clearly consistent with equation (4.4). The difference equations (4.7) and (4.8) involve derivatives

in one spatial direction only, and so the respective linear algebraic systems can be written in the following form

$$-A_k\tilde{\mathbf{u}}_{k-1} + B_k\tilde{\mathbf{u}}_k - C_k\tilde{\mathbf{u}}_{k+1} = E_k, \quad k = 0, \ldots, N-1,$$

which is a cyclic, tridiagonal system because of the periodic boundary conditions. There are many stable and efficient numerical algebraic methods to handle systems of this type; for example, a combination of the Sherman-Morrison formula [33] and a diagonal solver [23].

We now come to the second step of the projection method that maps the velocity field onto the space of divergence-free vector fields. A centered finite difference approximation of Poisson's equation can be written

$$(\mathbf{D}^+ \cdot \mathbf{D}^-\psi)(\mathbf{x}) = \mathbf{D}^0 \cdot \mathbf{u}^{**}. \tag{4.9}$$

After we compute the values ψ from the equation (4.9), we can update the fluid velocity using a discrete version of (4.6):

$$\mathbf{u}^{n+1} = \mathbf{u}^{**} - \nabla\psi. \tag{4.10}$$

This completes the specification of the discrete fluid equations on a Cartesian lattice.

In general, the efficiency of the IB method relies on a suitable method for solving the Poisson's problem (4.9). Depending on the physical problems of interest, a variety of different numerical solvers could be used to compute the pressure update, and a variety of numerical approaches have appeared in the literature in the context of immersed boundary problems. In our case, a massless elastic fiber is immersed in the uniform fluid with constant density. The problem (4.9) therefore has constant coefficients, which simplifies considerably the resulting linear algebraic system. In particular, Peskin described in [27] how an efficient Fourier transform methods works exceedingly well here. For more details about the technical implementation and fundamental theory of FFT, please refer to the books of Press [33, 34] and Strang [39].

Recently, many authors have been considering IB problems with variable coefficients, involving either massive boundaries or non-uniformly dense fluids. In both cases, the delta functions in the immersed boundary method take on the additional role of spreading mass within the fluid, and hence they appear in the expression for the fluid mass density. Fourier transform methods are not applicable to these problems, and possible alternative solution approaches include: (1) applying a multigrid technique to solve Poisson's problem with

variable density (see Zhu [41]); (2) retaining an FFT solver by attaching a ghost (or twin) boundary onto the physical by way of very stiff strings that distribute the gravitational force onto the fluid. This latter technique, called the Penalty Immersed Boundary method, was proposed by Kim and Peskin [15], and is very simple and easily transplanted to existing IB codes.

4.2 Immersed boundary component

4.2.1 Fiber force

We next describe how to discretize the immersed boundary force density which was introduced in Section 2.1, first reviewing some basic notation. The symbol s is used to denote the parametrization of points along the immersed boundary in Lagrangian coordinates; $\mathbf{X}_k(t)$ represents the spatial position of control (or marker) points on the boundary associated with the discrete immersed boundary point s_k, and denoted by index k. We denote by L the length of the immersed boundary in its equilibrium state. We also define N_b to be the number of Lagrangian points, and Δs to be the step in the arc-length parameter separation each discrete point along the fiber.

Since our computational domain is periodic in space, the arithmetic on indices is computed in k, modulo N_b. Based on the form (2.9) of the tension force corresponding to springs having zero resting length, we can discretize the second derivatives using centered second-order differences to obtain the approximation

$$\mathbf{F}_k = \kappa \, \frac{\mathbf{X}_{k+1} - 2\mathbf{X}_k + \mathbf{X}_{k-1}}{(\Delta s)^2}, \tag{4.11}$$

where κ is the dimensional stiffness defined in (2.6). This form of forcing is very commonly used in the literature, but in general, the resting length in the spring force may not be zero, for example, denoted to be $L_r = 1$. In this case, we need to discretize equations (2.5)-(2.8), which using the usual centered second-order differences can be approximated by

$$\begin{aligned} T_{k+\frac{1}{2}} &= \kappa \left(\frac{|\mathbf{X}_{k+1} - \mathbf{X}_k|}{\Delta s} - 1 \right); \\ \boldsymbol{\tau}_{k+\frac{1}{2}} &= \frac{\mathbf{X}_{k+1} - \mathbf{X}_k}{|\mathbf{X}_{k+1} - \mathbf{X}_k|}. \end{aligned}$$

Using these expressions, the discrete force density is given by

$$\mathbf{F}_k = \kappa \, \frac{T_{k+\frac{1}{2}} \boldsymbol{\tau}_{k+\frac{1}{2}} - T_{k-\frac{1}{2}} \boldsymbol{\tau}_{k-\frac{1}{2}}}{\Delta s}. \tag{4.12}$$

In this thesis, we will not implement this kind of force density in the computation of resonance and will restrict our attention to the form (4.11).

4.2.2 Interaction

We now come to the equations that connect the fluid and the immersed boundary. The internal boundary is moving along with the surrounding flow and changes its configuration continuously in time. Meanwhile, the deformation of the immersed boundary exerts a singular force onto the nearby fluid particles. As mentioned before, when the problem is discretized, the control points on the membrane generally do not coincide with the fluid lattice, and so fluid and fiber quantities cannot be transferred directly from one grid to the other; instead, the interaction between the two is mediated by Dirac delta functions. This feature requires us to give a smooth approximation to the delta function for the purposes of the numerical discretization. A typical smoothed delta function in one dimension is given as follows:

$$\delta_h(x) = \begin{cases} \frac{1}{4h}\left(1+\cos\frac{\pi x}{2h}\right), & |x| \le 2h, \\ 0, & \text{otherwise.} \end{cases} \tag{4.13}$$

The particular reasons for this choice of smoothed delta function are given in [27], and relate to the accuracy and stability of approximations for our particular choices of projection method and discrete mesh. Two-dimensional discrete delta functions are defined by forming products of one-dimensional delta functions as follows

$$\mathcal{D}_{ij}(\mathbf{X}) = \delta_h(X-x)\delta_h(Y-y) = \delta_h(X-ih)\delta_h(Y-jh), \tag{4.14}$$

where $\mathbf{X} = (X,Y)^T \in \Re^2$.

The role of the 2D delta function in terms of interpolating fiber force densities onto the fluid grid points is illustrated in Fig. 4.1. In the left hand picture, an immersed interface having a sinusoidal shape is represented by a set of control points 'o' in blue. They are embedded within a rectangular fluid region discretized on a uniform Cartesian grid, that is plotted with grey dotted lines. As shown, the fiber markers need not coincide with the fluid grid. When we apply the two-dimensional discrete delta function (4.14) to spread the fiber force from a specific fiber point (the filled-in circle in the figure) onto the fluid grid points '×' which are within a $4h$-by-$4h$ square centered on the fiber point labelled '•'. A two-dimensional representation of the smoothed delta function centered at the indicated fibre point is included in the right-hand picture of Fig. 4.1.

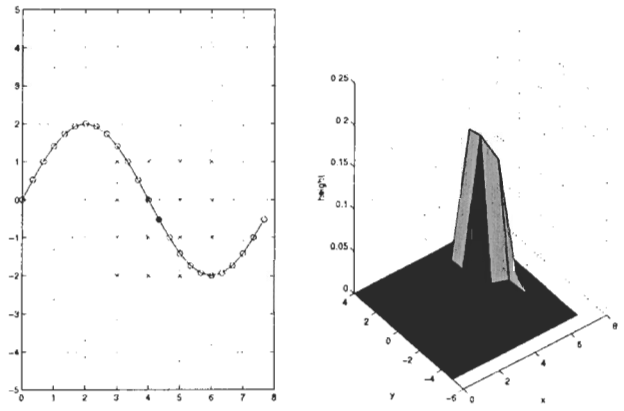

Figure 4.1: The relation between a control point and nearby grid points (left), and the corresponding cosine approximation to $\mathcal{D}(\mathbf{X})$ in (4.14) (right).

Our assumption of periodic boundary conditions requires us to take special care when extending delta functions across boundaries. Fig. 4.2 shows a specific example, where the fiber point under consideration, marked '•', is within two grid points of the right boundary, and so its influence is felt across the periodic boundary to the left side of the domain as well, as displayed in the right plot of Fig. 4.2.

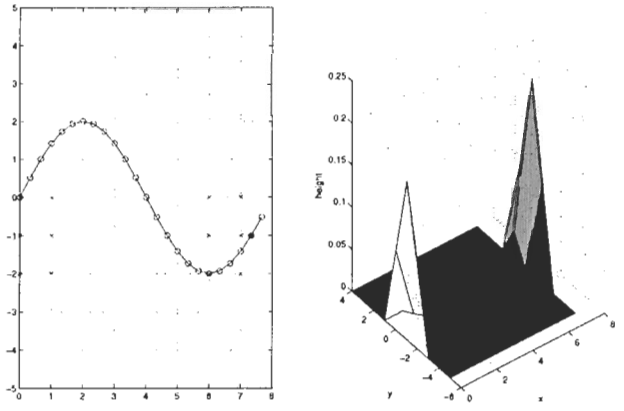

Figure 4.2: An example of a delta function interpolation step in which the periodic boundary condition must be taken into account.

Now we can describe the specific algorithms for computing the interaction terms. The

immersed boundary spreads the singular force at fiber points onto the surrounding fluid points as defined in (2.4). The force $\mathbf{f}_{ij}^n$ at a specific fluid grid point can be discretized as

$$\mathbf{f}_{ij}^n = \sum_{k=0}^{N_b-1} \mathbf{F}_k^n(\mathbf{X}_{k-1}^n, \mathbf{X}_k^n, \mathbf{X}_{k+1}^n)\, \mathcal{D}_{ij}(\mathbf{X}_k^n)\, \Delta s, \tag{4.15}$$

where the fiber density $\mathbf{F}_k$ is given in (4.11).

The delta functions also serve to interpolate the velocity at the marker points $\mathbf{X}_k$ on the interface using fluid velocities $\mathbf{u}_{ij}^n$. The continuous interpolation formula for the interface velocities in (2.3) can be approximated by

$$\mathbf{U}_k^n = \sum_{i,j=0}^{N-1} \mathbf{u}_{ij}^n\, \mathcal{D}_{ij}(\mathbf{X}_k^n)\, h^2, \tag{4.16}$$

where $\mathbf{U}_k$ corresponds to the velocity at the control point s_k of the immersed boundary. Then, the no-slip boundary condition, which is simply an evolution equation for the immersed boundary points, can be approximated by

$$\mathbf{X}_k^{n+1} = \mathbf{X}_k^n + \Delta t\, \mathbf{U}_k^n. \tag{4.17}$$

We should emphasize that we have chosen time indices in the above discrete equations so that the force spreading and velocity interpolation steps are fully explicit. We could adjust the time index on certain quantities in the equations (4.15)-(4.17) to obtain a variety of other implicit time discretizations. In this thesis, we will consider the explicit algorithm only.

4.3 Computing algorithm

Assuming that a massless elastic fiber is immersed in a viscous incompressible flow having uniform density, the explicit algorithm takes the following form:

- **Initially:** We assume we have the boundary position $\mathbf{X}^n$ at the control points of the membrane, and the velocity field $\mathbf{u}^{n-1}$ of the fluid from the previous time step.
- **Step 1.** Evaluate the fiber force density $\mathbf{F}_k^n$ at each control point $\mathbf{X}_k^n$ of the interface, using equation (4.11), which can be written in the alternate form

$$\mathbf{F}_k^n = \kappa\, (D_s^+ D_s^-)(\mathbf{X}_k^n).$$

- **Step 2.** Use $\mathbf{F}_k^n$, to spread the singular fiber force onto the fluid lattice, using the discrete delta function (4.14) and the discretization for fiber force (4.15):

$$\mathbf{f}_{ij}^n = \sum_{k=0}^{N_b-1} \mathbf{F}_k^n \, \mathcal{D}_{ij}(\mathbf{X}_k^n) \, \Delta s.$$

- **Step 3.** Use $\mathbf{f}^n$ and $\mathbf{u}^{n-1}$, to solve the Navier-Stokes equations with the projection method and fast Poisson solver that update the velocity of fluid to obtain a divergence-free field $\{\mathbf{u}_{ij}^n\}$ at the next time step.

- **Step 4.** Interpolate the fluid velocities to obtain velocities $\mathbf{U}_k^n$ at fiber points using

$$\mathbf{U}_k^n = \sum_{i,j=0}^{N-1} \mathbf{u}_{ij}^n \, \mathcal{D}_{ij}(\mathbf{X}_k^n) \, h^2.$$

- **Step 5.** Use $\mathbf{U}_n$ to move the control points on the immersed boundary to their new positions:

$$\mathbf{X}_k^{n+1} = \mathbf{X}_k^n + \Delta t \, \mathbf{U}_k^n.$$

This completes a single time step, and the algorithm repeats by returning to Step 1.

Chapter 5

Numerical Results

In this chapter, we present numerical results for several test problems that indicate the stability and convergence properties of the IB method that we have implemented. We then investigate in detail parametric resonances that appear in the forced flat fiber.

5.1 Stability and convergence

In order to ascertain the stability and convergence of the IB method, we consider a simple test problem consisting of an elliptical membrane under tension that is immersed in a viscous incompressible fluid.

Example 5.1. This example is taken from Tu and Peskin [40], LeVeque and Li [22], and Lee [19], and is illustrated in Fig. 5.1. The initial state of the membrane is an ellipse with major and minor axes $a = 0.75$ and $b = 0.5$. The elastic membrane has fluid both inside and out, and both fluids have constant density $\rho = 1.0$. The unstretched state of the membrane is taken to be a circle of radius $r = 0.5$, but because the fluid is incompressible and the membrane does not leak, the actual equilibrium state is a circle of radius $r_e = \sqrt{ab} \approx 0.61237$ (where r_e is such that the volume is identical to that contained within the initial membrane).

In our computations, the fluid domain is taken to be the square, $[-1,+1] \times [-1,+1]$, having periodic boundary conditions. The restoring force is taken of the form (4.12) with constant stiffness, κ. In general, the membrane can return to its equilibrium position in one of two ways: (1) relaxing monotonically to the equilibrium circular state which happens

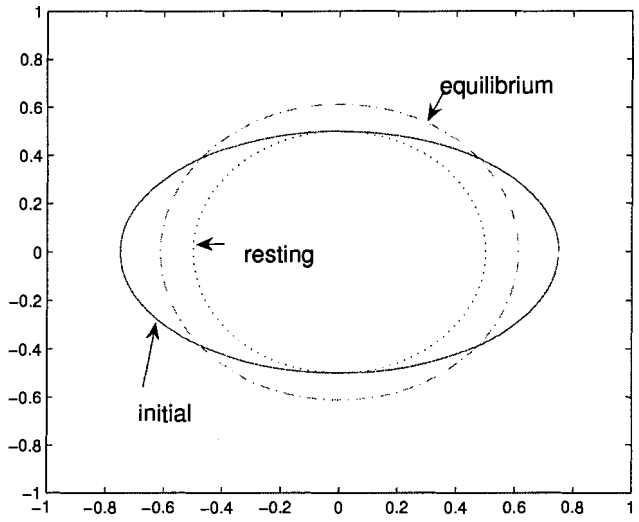

Figure 5.1: The interface configuration, showing the initial membrane of the initial ellipse (red solid line), the circular equilibrium state (green dash-dot line), and the smaller unstretched state (blue dot line.)

when the Reynolds number Re is small, say $Re < 1$ (the case of Stokes flow was considered previously in [22]); or (2) oscillating around the equilibrium state, when the Reynolds number is larger, for instance of $Re > 100$. For the case of Reynolds number Re falling in the middle range, we could not determine the way of the membrane motion because either of them could happen here. In this section, we will focus on the latter case involving an oscillating interface.

Fig. 5.2 plots the variation in the radius over time for various choices of the grid resolution (indicated by N for an $N \times N$ grid) and the number of fiber control points, N_b. Unless otherwise specified , our computations assume $N_b = N$. Let r_x and r_y be the semi-major and semi-minor axes respectively of the elliptical interface at the instant when the maximum extension is reached.

In this example, the Reynolds number is taken to be approximately $Re = 105$ so that both radii, r_x and r_y, will oscillate about the equilibrium radius $r_e = 0.61237$ but eventually relax towards this equilibrium state owing the presence of damping. In all cases, we observe a problem with loss of volume, which is well-known for the present IB method. The size of the volume error can be reduced by refining the mesh, which is clearly seen by comparing

to the $N = 256$ calculation. Peskin and Printz [32] also suggested a modification to the leaking problem by introducing a modified projection operator, but we will not implement this here.

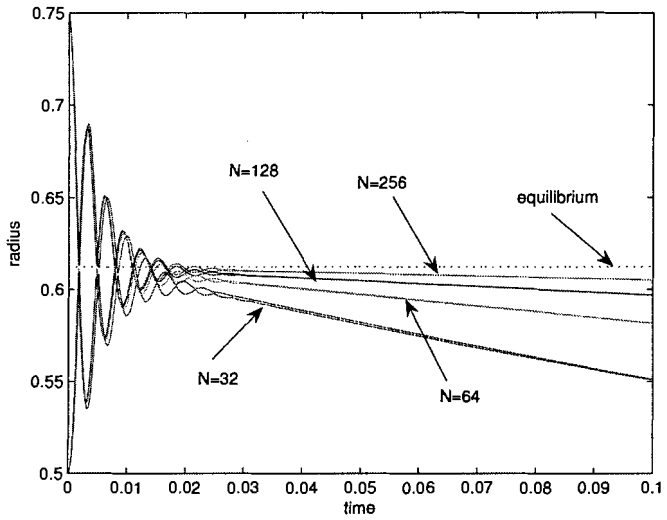

Figure 5.2: A comparison of the computed radius on an $N \times N$ grid with $N_b = N$ control points in the interface. The solid lines represent the semi-major and semi-minor radius and are displayed in colors corresponding to the following pairs of N(color): 32(magenta), 64(blue), 128(red), 256(green).

One-dimensional slices can be drawn of the computed velocity to show the stability of the IB method in response to grid refinement. For example, in the bottom picture of Fig. 5.3 we present the u-component of velocity at $y = -0.2656$ and $t = 0.1$. The computation is based on a 64×64 grid and $N_b = 64$ boundary points. In contrast with what we have seen so far of the fluid velocity crossing the interface in Section 2, the profile of u-velocity here is not as smooth as might be expected. Fig. 5.3 indicates that on either side of the boundary the fluid velocities take on opposite signs, and this singularity owes to the particular choice of discrete delta function used in our IB method. If the grid is refined, then the corresponding change in the velocity profile can be observed in Fig. 5.4, wherein the singularity in velocity is confined to a narrower and narrower band as N is increased. This figure also shows that the velocities on both sides of the immersed boundary take the same sign in the cases $N = 128$ and 256. In recent years, several methods have been developed to increase the accuracy of the method, such as with the Immersed Interface Method or variants [22, 20].

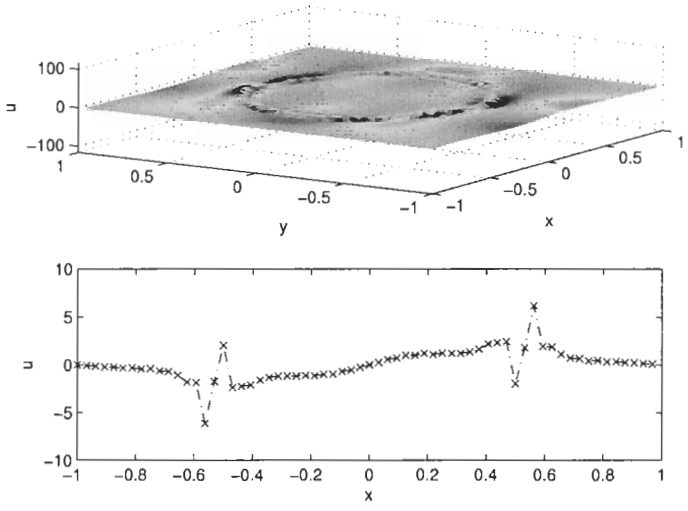

Figure 5.3: The plot on top is a surface plots of the u-component of the fluid velocity, and the bottom plot shows a 1D slice at $y = -0.2656$. The grid is chosen to be 64×64 and $t = 0.1$ in both cases.

This approach reformulates the delta function forcing in terms of jump conditions across the membrane, but it is significantly more complicated than the IB method, particularly in three dimensions.

Next we investigate the accuracy and convergence properties of the IB method. Since the fluid is incompressible, and the immersed boundary obeys the no-slip condition, the volume (or area in 2D) enclosed by the interface should be exactly conserved; we can therefore use the enclosed area V_N computed from the current interface location as one measure of the accuracy of the IB method. Table 5.1 shows the relative error in area for a number of grid refinement levels. The area enclosed within the boundary on three different fluid meshes (of size $N \times N$, with $N = 128$, 64, and 32) are compared with a finest mesh solution with $N = 256$, and the respective errors are measured in the max-norm using the following formula

$$ratio = \frac{||V_{N/2} - V_{256}||}{||V_N - V_{256}||}.$$

Because we are using a 256×256 grid to calculate the error instead of using the exact solution or a much finer resolved calculation, we do not expect the ratio of successive differences to be equal to the standard ratio of 2 for a first order scheme or 4 for the second-order one.

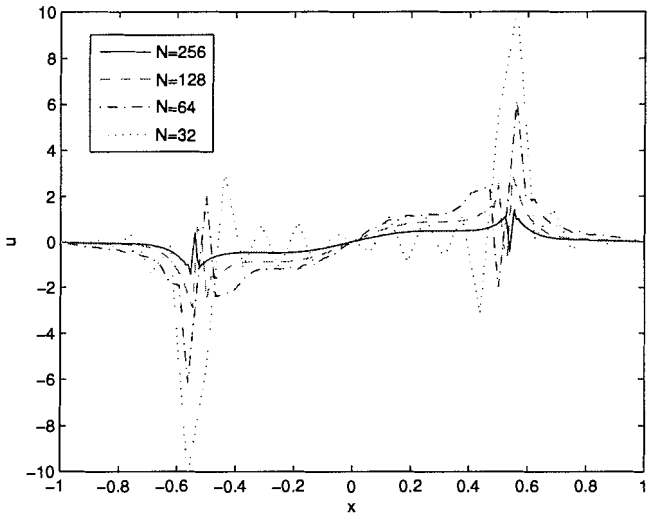

Figure 5.4: A series of 1D slices through the u-velocity at $y = -0.2656$ and $t = 0.1$. The curves with different color and line style correspond to different choices of $N \times N$ fluid grid, with the value of N reported in the legend.

Instead, the ratio for a q-th order method will be

$$ratio \approx \frac{C(2^{-N})^q - C(2^{-8})^q}{C(2^{-(N-1)})^q - C(2^{-8})^q},$$

according to the above equation, which for the first order scheme ($q = 1$) equals $\frac{4-1}{2-1} = 3$ for $N = 128$ and $\frac{8-1}{4-1} = 2.3$ for $N = 64$ respectively. The computed ratios are listed in Table 5.1 and displayed graphically in Fig. 5.5, which support the well-accepted conjecture that the IB method is first-order accurate in space (similar results have been reported in [22, 20, 30]).

N	256	128	64	32
$\|\|V_N - V_{256}\|\|_{max}$	-	0.0316	0.0881	0.1970
ratio	-	2.7871	2.2350	-

Table 5.1: The relative errors in volume conservation at $t = 0.1$, demonstrating the first-order accuracy of our IB method.

Besides the accuracy measured by volume conservation in the max-norm, we can also consider the error of the entire interface location in the 2-norm, which was used in [22]. The

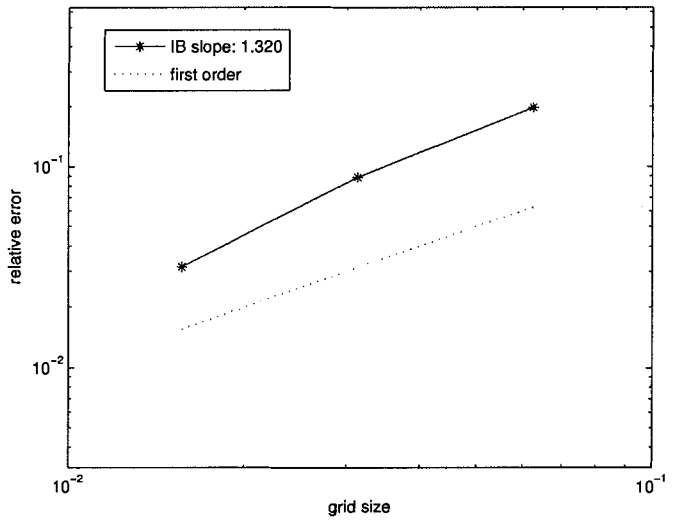

Figure 5.5: Grid refinement study showing relative errors in volume conservation at $t = 0.1$. The plot accompanies the Table 5.1 to demonstrate the first-order accuracy of our IB method.

error was defined as

$$e_N = \sqrt{\sum_{i=0}^{N_b-1} \left(X_i^{(N,N_b)} - X_{i^*}^{(N^*,N_b^*)}\right)^2 + \left(Y_i^{(N,N_b)} - Y_{i^*}^{(N^*,N_b^*)}\right)^2},$$

where the set $\{\mathbf{X}\}_{i=0}^{N_b-1} = \{(X_i, Y_i)\}$ denotes the positions of control points on the interface; (N, N_b) is a pair of the numbers representing the fluid grid and boundary markers, and the pair (N^*, N_b^*) denotes the finest mesh. For the purposes of matching the control points $\{i\}$ on coarse grids (N, N_b) to those $\{i^*\}$ on the finest grid (N^*, N_b^*) exactly, we must require that N_b always divides $N_b^* = 256$, which allows a direct comparison of control points with the finest grid solution. In Fig. 5.6, we plot the relative global errors at $t = 0.1$ relative to the finest grid ($N^* = 256, N_b^* = 256$). Other pairs (N, N_b) used here include $(32, 32)$, $(32, 64)$, $(64, 64)$, $(32, 128)$, $(64, 128)$, and $(128, 128)$, that correspond to the points '$*$' sorted from right to left in Fig. 5.6. The test results show that the definition e_N provides an appropriate error measure for the interface location, and that our IB method converges as expected (with first-order accuracy) in this error norm.

Another thing we can see in Fig. 5.6 is that there is a sharp drop in the error when N_b increases from 64 to 128. In comparison to the points $(64, 64)$ and $(32, 128)$, both of

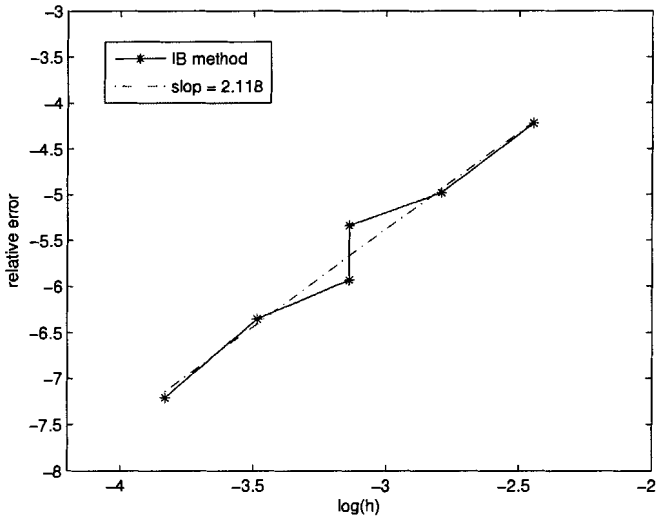

Figure 5.6: The global error e_N against the refined mesh $h = 1/\sqrt{h * \Delta s} \sim 1/\sqrt{N * N_b}$, measured along the entire interface at $t = 0.1$, which demonstrate the expected first-order convergence in our IB method.

them hold the same magnitude of $log(h) \sim 1/2^{12}$, but the point $(32, 128)$ results in much less relative error as indicated by the sharp drop in Fig.5.6. It implies that the number of control points N_b in the interface is more significant than the number of fluid grid points N in the error of IB method. For details, please refer to [22]. In practice, this suggests that we must refine both the fluid domain and the interface simultaneously in order to increase the accuracy of IB method.

Before we move on to the next example, we will address the advantages and disadvantages of the IB method. The most outstanding feature of the IB method is its use of discrete δ-functions to interpolate between grids, and both advantages and disadvantages derive from this. In summary, the advantages of IB method are:

- simplicity and ease of implementation;
- flexibility in dealing with complex geometry;

and disadvantages:

- first-order accurate;

- errors in volume conservation due to fluid "leaking" between immersed boundary points.

Those limitations were already addressed in the previous example, and corresponding strategies to overcome these limitations have been discussed. We will nonetheless restrict our computations to this simple first order implementation.

5.2 Unforced circular fiber

In this section, we look at one of the "standard" examples consisting of an elastic circular fiber under the influence of small perturbations. No other applied force is exerted on fiber, except for the intrinsic restoring spring force in the fiber, whose force density is given as (4.11) with a constant stiffness. This problem was analyzed before in the inviscid case by Cortez and Varela in [7], who derived asymptotic solutions. Cortez, Peskin, Stockie and Varela [8], on the other hand, investigated the stability of an unforced fiber in a viscous fluid (although the bulk of their results corresponded to the periodically-forced case). These two sets of analytical results will be used here to compare with our numerical simulations.

Example 5.2. We take a closed fiber immersed in a viscous fluid which has an equilibrium state that is a circle of radius $r_e = 0.5$. We let the resting length be $r_0 = 0$ so that the fiber would shrink to a point in the absence of fluid lying inside the fiber. An initial perturbation is imposed on the circular fiber, given in polar coordinates as

$$r(\theta, t) = r_e + r_\epsilon \cos(\wp\theta),$$

where $r_\epsilon = r_e/10$ denotes the amplitude of the perturbation, and the wavenumber $\wp$ is an integer. Fig. 5.7 shows a circular fiber perturbed with the wavenumber $\wp = 3$.

In [8], the authors gave an asymptotic expression for the radius of a perturbed circular fiber in dimensionless variables

$$r(\theta, t) = 1 + \epsilon B(t) \cos(\wp\theta) + O(\epsilon^2), \tag{5.1}$$

where $\epsilon = r_\epsilon/r_e$ and $B(t)$ was assumed to have the form

$$B(t) = e^{\alpha t}[\cos(\beta t) + \frac{\alpha}{\beta} \sin(\beta t)].$$

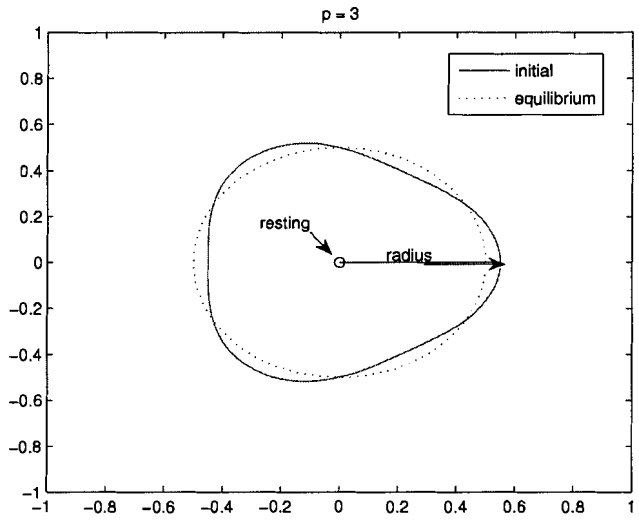

Figure 5.7: The circle interface perturbed by a mode with wavenumber $\wp = 3$.

The parameters α and β represent respectively the decay rate and frequency of the resulting oscillations in time, and they represent a convenient means to compare the analytical and computed results.

This approach was employed in [8], wherein a linear system was derived for the interface location $\mathcal{X}$

$$\mathcal{D}\left(\sqrt{\frac{\lambda}{\nu}};\, \phi, \wp\right) \mathcal{X} = 0, \tag{5.2}$$

where $\phi = \nu^2/\sigma$ and $\lambda := \alpha + i\beta$ is the Floquet multiplier defined in (3.11). In fact, the system (5.2) plays the same role as the equations (3.21) and (3.22) in this thesis. A non-trivial solution exists if and only if the determinant $det\,(\mathcal{D}) = 0$, which yields an implicit function for λ as a function of the other parameters. Instead, we can express the determinant condition in the following explicit form

$$\frac{\alpha}{\sqrt{\sigma}} + i\frac{\beta}{\sqrt{\sigma}} = F\left(\phi, \wp\right). \tag{5.3}$$

If we select a specific wavenumber $\wp$, then the values $\alpha/\sqrt{\sigma}$ and $\beta/\sqrt{\sigma}$ can be computed for a series of parameters ϕ by evaluating (5.3) numerically. The results corresponding to $\wp = 3$ are shown in Fig. 5.8.

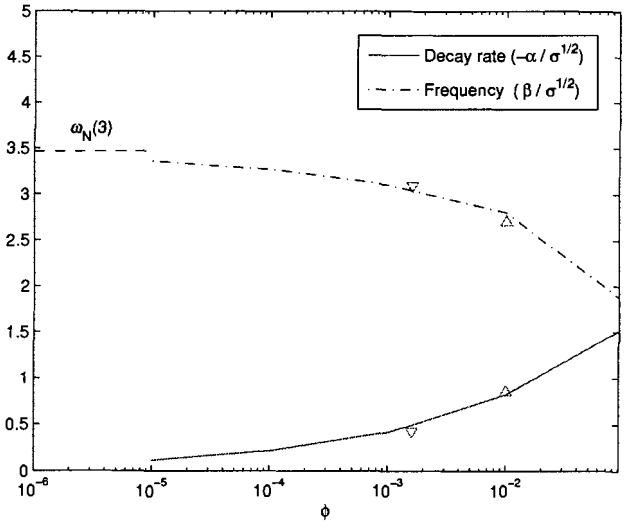

Figure 5.8: Plots of decay rate α and frequency β versus ϕ, for the $\wp = 3$ wavenumber. The vertical axis gives scaled values of α and β calculated from the dispersion relation, $det\,\mathcal{D} = 0$. The zero-viscosity ($\phi = 0$) limit is also displayed for the frequency, which can be shown to reduce to $\omega_N(\wp) = \sqrt{\wp(\wp^2 - 1)/2}$. Two sets of numerically computed results are shown for comparison purposes, corresponding to the values $\phi = 10^{-2}$ and $\phi = 1.6 \times 10^{-3}$.

Putting together the asymptotic formula in (5.1) along with our estimates of α and β from Fig. 5.8, we can write down an explicit approximation of the radius as a function of angle θ and time t for comparison purposes. The motion of the immersed boundary point located at $\theta = 0$ is plotted in Fig. 5.9 for $\phi = 10^{-2}$ and in Fig. 5.10 for $\phi = 1.6 \times 10^{-3}$. The two groups of parameters are listed in Table 5.2. We observe that the computed results agree very well with the analytical result in both cases, which confirm the validation of the computations in our IB method.

Group	1	2
Fig.	5.9	5.10
α	0.85	0.43
β	2.7	3.1
ϕ	1.0×10^{-2}	1.6×10^{-3}
ν	0.3405	11.5942
σ	0.1608	17.6404

Table 5.2: Parameters corresponding to the unforced circular fiber considered in Example 5.2.

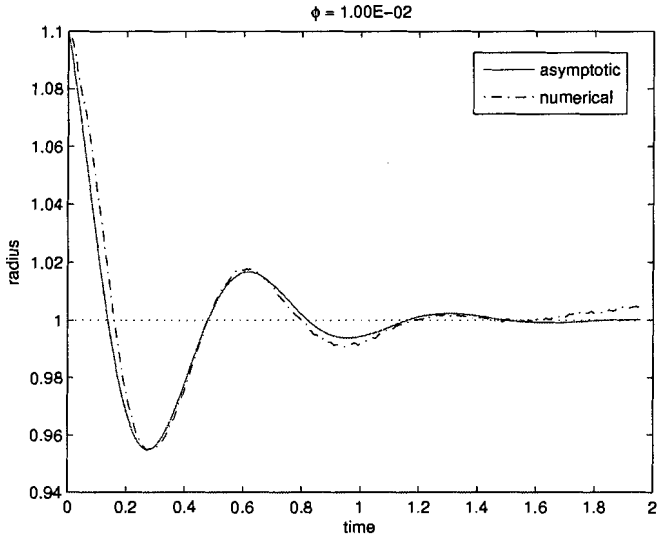

Figure 5.9: Group 1: Comparison of the analytical and numerical solutions for Example 5.2 with $\phi = 10^{-2}$.

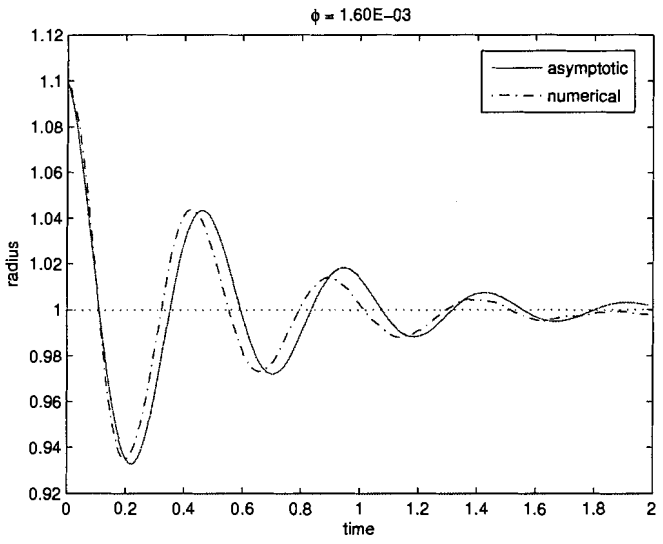

Figure 5.10: Group 2: Comparison of the analytical and numerical solutions for Example 5.2 with $\phi = 1.6 \times 10^{-3}$.

5.3 Parametric resonance in a flat fiber

In comparison with the results for the circular fiber just described, we will now present numerical results to demonstrate the validity of the Floquet analysis in Chapter 3 and the existence of parametric resonance for an elastic fiber that is perturbed from a horizontal or "flat" equilibrium state. Our computations are performed by implementing the explicit algorithm for the IB method described in Chapter 4. Some interesting numerical results regarding the resonant modes in the flat fiber are included at the end.

Example 5.3. Our computational domain is a square box, $[0,1]\times[-\frac{1}{2},\frac{1}{2}]$, with periodic boundary conditions applied in both co-ordinate directions. A horizontal elastic fiber is placed in the center of the square box along $y = 0$, as shown in Fig. 2.1. The fiber is initially given a vertical perturbation of the form $y = 0.05\cos(2\wp\pi x)$, where $x \in [0,1)$ and $\wp$ is the wavenumber. Our numerical simulations are performed with a 64×64 fluid grid and with 192 control points along the interface, and we also compute on a finer grid of dimension 128×128, with 384 immersed boundary points, to ensure the accuracy of the results. The time step in all cases is chosen well within the stability restriction imposed by our explicit method to avoid any problems with simple numerical instabilities.

We choose four sets of parameters that the analysis in Section 3.5 suggests will lead to

parametric resonance. The parameters are chosen in such a way that a different wavenumber $\wp = 1, 2, 3, 4$ is excited in each case (numbered respectively I, II, III, IV); all parameter values are listed in Table 5.3. In computations, we vary only the frequency ω_0 of the modulating stiffness (2.6) and hold all other parameters fixed. The dimensionless parameters σ and ν are calculated from equations (2.16), and can be used to draw the eigenvalue plots. For example, Figs. 3.3 and 3.4 presented earlier in Chapter 3 depict the stability regions for Cases II ($\wp = 2$) and IV ($\wp = 4$). In both of these cases, the first unstable tongue corresponds to the harmonic mode of oscillation.

In Fig. 5.11, we present numerical evidence to support the existence of parametric resonance in the four cases. In this figure, the plots are arranged in the following order within each row:

1. Left plot: the initially fiber position, perturbed in the $\wp$th wavenumber.
2. Middle plot: eigenvalue plot from the Floquet analysis which determines the lowest unstable mode.
3. Right plot: numerically computed amplitude of the unstable $\wp$-mode.

Case	I	II	III	IV
mode($\wp$)	1	2	3	4
σ	6.9e-3	9.9e-4	3.6e-4	1.8e-4
ν	5.9e-4	2.2e-4	1.3e-4	9.4e-5
ω_0	1700	4500	7500	10600
L	1.0			
ρ	1.0			
μ	1.0			
ϵ	0.45			
κ_c	20000			

Table 5.3: Parameters for four resonant cases, having a lowest unstable mode with wavenumber $\wp$ varying from 1 to 4.

In each case, the plots indicate that when internal forcing is applied via periodic variations in the stiffness parameter – where the frequency is chosen to be the resonant frequency suggested by the analysis – then the amplitude of oscillation grows far beyond that of the

Case I:

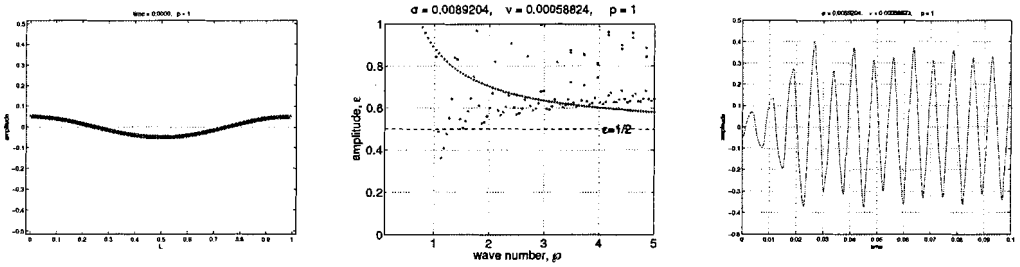

Case II:

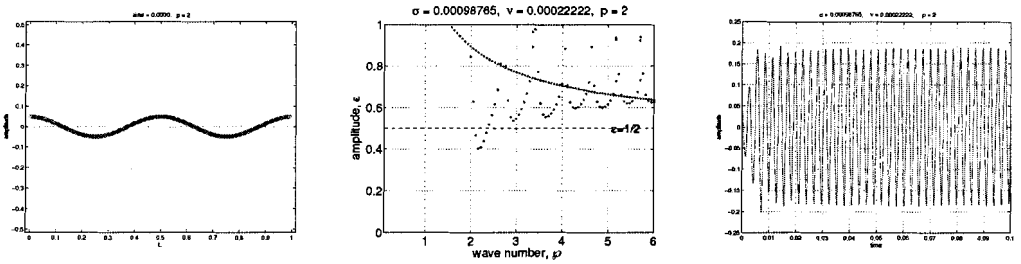

Case III:

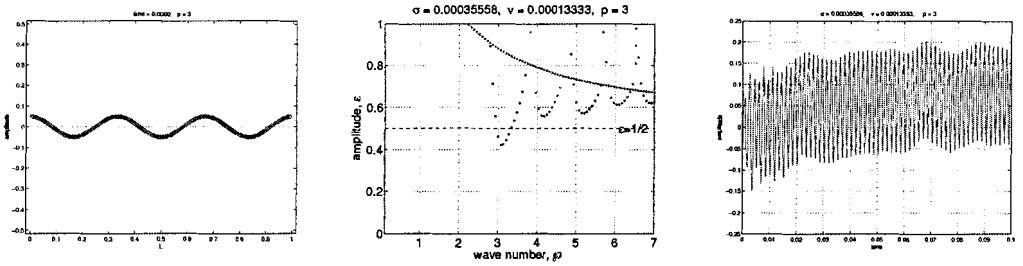

Case IV:

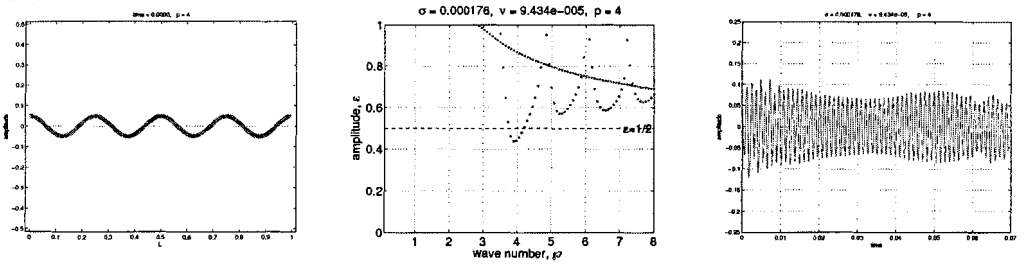

Figure 5.11: A series of plots for four cases in Table 5.3 showing the analytical and numerical comparison of parametric resonance in the unstable $\wp$-mode. In each case, the *left* plot gives the initial state of perturbed fiber; the *middle* plot presents the stability diagram from the Floquet analysis; and the *right* plot shows the computed amplitude of the resonant $\wp$-mode.

initial perturbation, 0.05 cm. Although the immersed boundary motion never becomes unbounded, the fiber does exhibit sustained, large-amplitude oscillations. There are a number of explanations for why the fiber motion remains bounded instead of exhibiting true instabilities:

- The artificial viscosity introduced by the first-order scheme damps the amplitude of oscillations in the interface.
- The equations are linearized in the analysis, that drops out the non-linear convection terms as well as the nonlinearities in the fiber force. The simplified system becomes more stable.
- The analysis assumes the domain is infinite in the vertical direction, but computations assume periodic boundary conditions. As a result, periodic copies of the fiber may interfere with each other and so reduce the oscillations.

Despite these discrepancies, the numerical computations still match the analytical results very well, which supports the existence of parametric resonance. For comparison purposes, we present the amplitudes of the unforced fiber for each cases in Fig. 5.12.

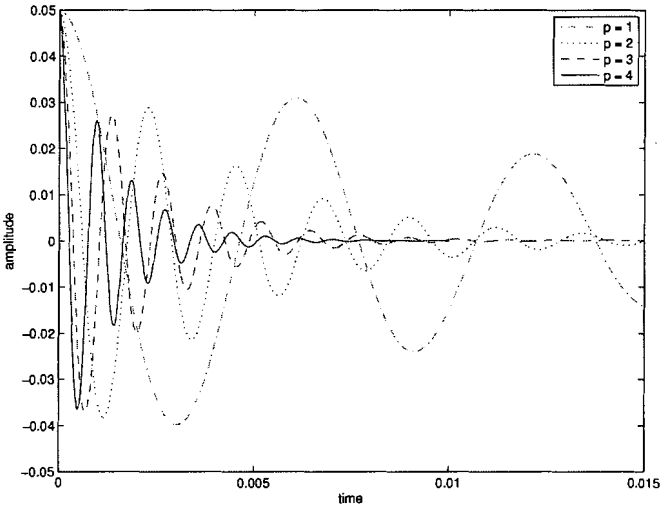

Figure 5.12: The amplitude of the unforced fiber for all cases in Table 5.3.

Next, we aim to validate the results of our analysis in Chapter 3 by investigating numerically the migration of the unstable tongues when we vary system parameters. This

will provide convincing evidence that the resonant behavior found earlier actually does arise from parametric resonance. Consistent with our earlier discussions in Chapter 3, we have chosen to consider Cases II and IV, so that numerical simulations are based on the same values of σ and ν as in the stability diagrams in Figs. 3.5 and 3.6.

At first, we vary the value of κ_c in the Case II to see the influence of changes in fiber stiffness on the amplitude of oscillation. As we saw in Fig. 3.5, the unstable $\wp = 2$ mode moves out of the unstable tongue whenever we increase or decrease the stiffness, κ_c, in which case 2-mode can no longer be excited and the perturbed fiber becomes stabilized. Fig. 5.13 exhibits the expected behavior as oscillations die out when we vary the stiffness significantly away from the resonant value.

Alternatively, if the viscosity is increased in Case IV, the oscillations should either decrease in amplitude or stop altogether, as suggested by the eigenvalue plots in Fig. 3.6. On the other hand, a decrease in viscosity might serve to increase the amplitude of the resonant oscillations. The respective numerical results are given in Fig. 5.14.

For Case I, Fig. 5.15 displays the effect of varying the stiffness perturbation amplitude, ϵ, on the resulting amplitude of oscillation. When $\epsilon \leq 3.0$, there is no longer any sustained resonance in the flat fiber.

In summary, the Floquet analysis suggests a very well-defined resonant frequency that results in a sustained, large-amplitude oscillation in numerical simulations. Furthermore, the corresponding instability can be predicted using the eigenvalue plots obtained from the Floquet analysis.

Before we finish this section, we would like to describe an interesting phenomenon that happens for odd unstable modes, and in particular for $\wp = 3$. As shown in Case III of Fig. 5.11, the resonant oscillations depart from the equilibrium state and no longer oscillate symmetrically about $y = 0$. This is different from resonances appearing in the other three cases, where the immersed interface exhibits large amplitude oscillations that are centered symmetrically about the equilibrium state. Refined computations are performed on a 128×128 fluid grid, with 384 fiber points (thereby doubling the computational time). A plot of the resonant amplitude versus time is shown in Fig. 5.16 with the $\wp = 3$ unstable mode. We observe that the motion of the interface appears to be composed of a mixture of the predicted $\wp = 3$ mode along with a number of other lower wavenumber modes. The boundary points are still oscillating at the high frequency predicted by the analysis, but there are additional lower-frequency oscillations not predicted by the analysis that are superimposed on the $\wp = 3$

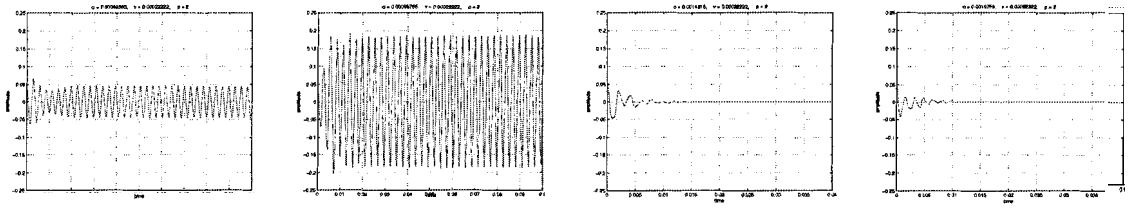

$\kappa_c = 10000$ $\kappa_c = 20000$ (Case II) $\kappa_c = 30000$ $\kappa_c = 40000$

Figure 5.13: A series of plots showing the impact of the changes in *stiffness* on the amplitude of oscillation for the Case II with resonant stiffness, $\kappa_c = 20000$. The various stiffness values are chosen to be the same as in Fig. 3.5.

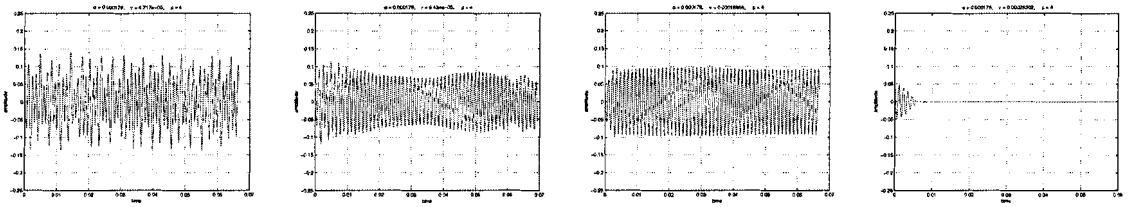

$\mu = 0.5$ $\mu = 1.0$ (Case IV) $\mu = 2.0$ $\mu = 3.0$

Figure 5.14: A series of plots showing the impact of changes in *viscosity* on the amplitude of oscillation for Case IV. The values of viscosity, μ, are chosen to be the same as those in Fig. 3.6.

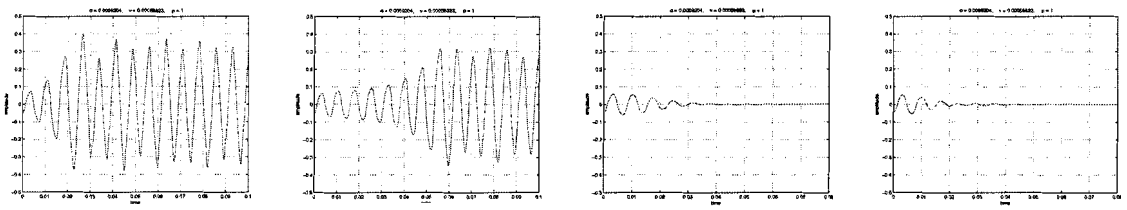

$\epsilon = 0.45$ (Case I) $\epsilon = 0.35$ $\epsilon = 0.30$ $\epsilon = 0.25$

Figure 5.15: A series of plots showing the impact of changes in *stiffness perturbation amplitude* on oscillations of the fiber for the Case I. As the forcing is reduced, the amplitude of the resonant oscillation also diminishes.

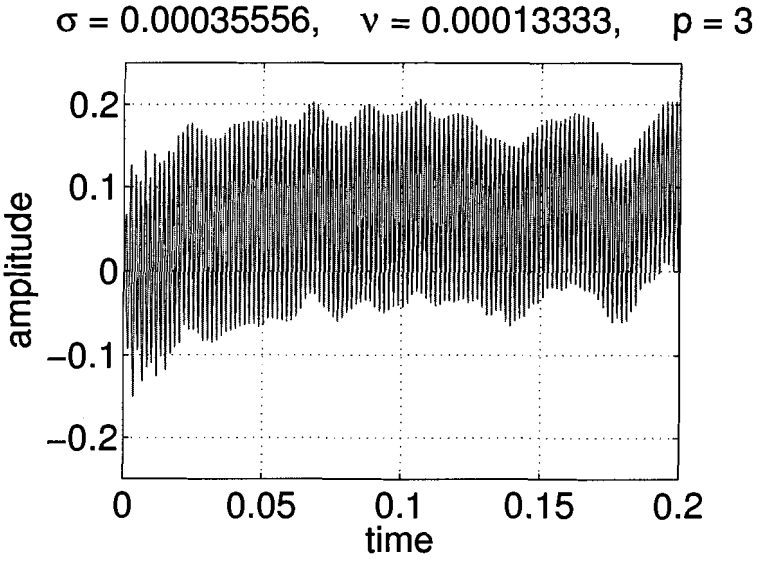

Figure 5.16: The amplitude of the resonant $\wp = 3$ mode on the refined 128×128 fluid grid with 384 boundary points. Besides the large-amplitude, high-frequency oscillations, there are also lower frequency oscillations superimposed on the interface motion.

mode and which cause the boundary to vary significantly from the analytical prediction. The forced fiber begins to oscillate in the $\wp = 3$ mode, then reduces to something approaching a wavenumber $\wp = 1$ oscillation near time $t = 0.07$. The $\wp = 3$ mode appears to be nearly recovered by time $t = 0.16$.

In the forced circular fiber, resonance at the odd unstable mode was not reported in [8], and so we don't know whether the oscillations with this transfer between modes could happen in the circular membrane or not. At present, we only display the numerical evidence of this interesting phenomenon and leave its analysis for future work.

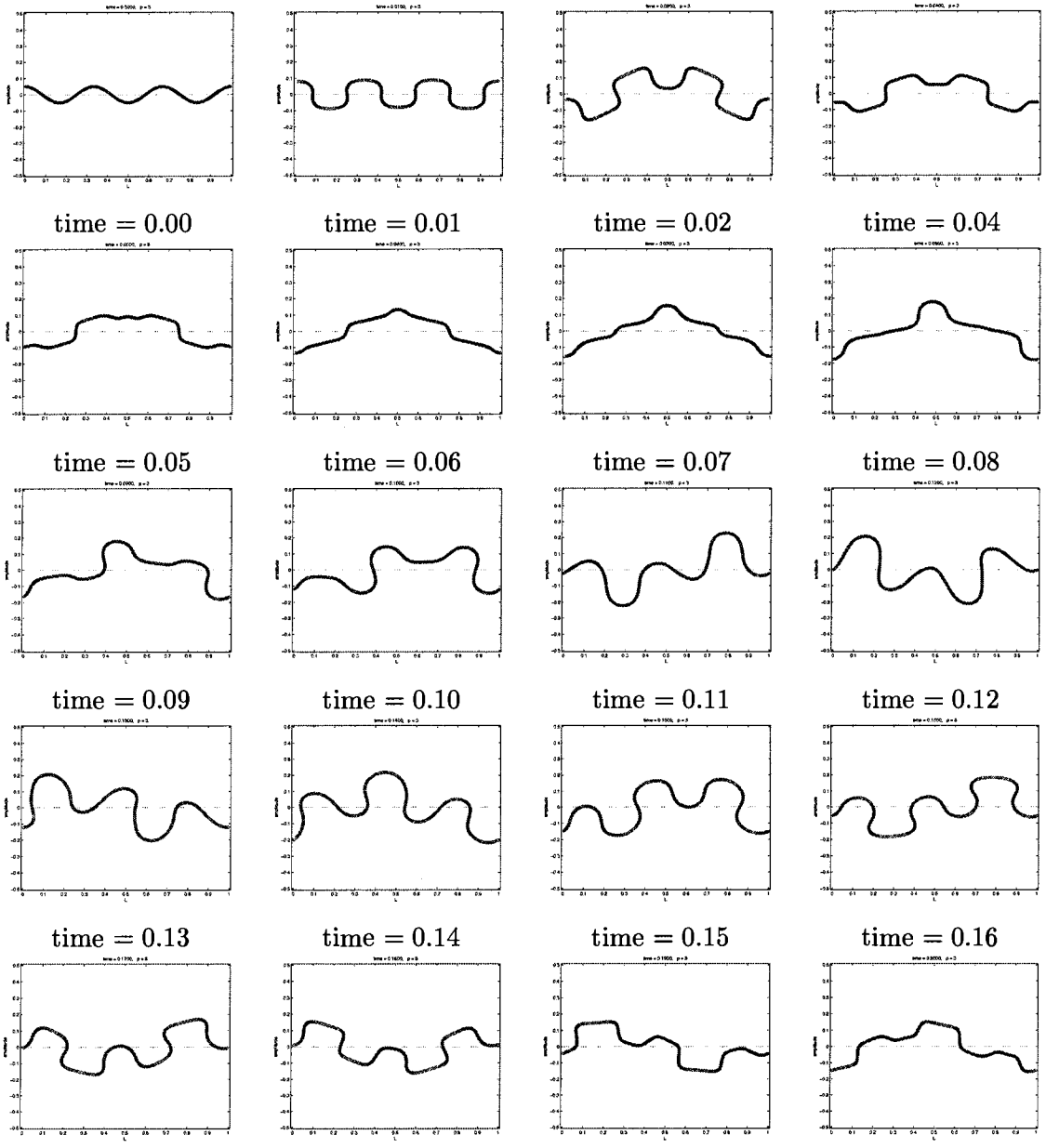

Figure 5.17: Resonant immersed boundary at the $\wp = 3$ wave mode for the Case III, computed on the refined 128×128 fluid grid with 384 boundary points. In the resonant oscillation, the unstable mode transfers from $\wp = 3$ to $\wp = 1$ at time = 0.07, then recovers back to $\wp = 3$ mode at time = 0.16, which indicates the existence of mode transformation in parametric resonance of the flat fiber.

Chapter 6

Conclusions and Outlook

6.1 Thesis contribution

The key contribution of this thesis is to study the instability of parametric resonance arising in a flat elastic fiber immersed in fluid governed by the 2D Navier-Stokes equations. This extends other previous work that had studied the stability of immersed boundaries in a circular geometry. The parametric resonance is driven by internal forcing that arises from periodic variations in the material stiffness parameter. The underlying mathematical model employs the linearized IB method, formulated in terms of jump conditions across the boundary. Assuming a horizontal interface with small perturbations, a Floquet analysis leads to an eigenvalue problem whose solution is similar in form to that for the circular interface but is nonetheless significantly simpler in its details. The stability of the solution is represented by regions in parameter space whose boundaries we derive analytically. Changes in parameters cause the stability regions (or "tongues") to migrate in the plane in a very predictable way. We also demonstrate numerically a phenomenon which is not predicted by the analysis wherein an odd resonant mode (with wavenumber $p = 3$) spontaneously generates additional lower-wavenumber modes and leads to much more complicated motion. Numerical simulations are presented to verify the existence of parametric resonance in a flat fiber.

The results in the thesis demonstrate that Floquet analysis is an extremely useful tool in examining parametric resonance and the unstable behavior of a broad class of problems

in fluid-structure interaction. Simultaneously, the consistency between numerical and analytical results for both flat and circular interface geometries has shown that the immersed boundary method is an efficient approach to capture not only the deformations of the elastic structure but also the motion of the surrounding fluid.

6.2 Future work

There are two main avenues for future research: one being in extending the stability analysis to other more complex problems in fluid-structure interaction; and the other is to applying the results to specific applications from the real world. We plan to extend the analysis to more realistic immersed boundary model, including a spatially-dependent stiffness, $\kappa(s,t)$, which is an important extension for dynamics of certain biological systems (such as the heart or the basilar membrane in the inner ear). However, this form of stiffness complicates the Floquet analysis significantly by coupling together the various wavenumbers, and therefore would require an extension of the current analytical method.

One of the most promising applications of this modified analysis is to the basilar membrane in the cochlea, which has a stiffness that varies exponentially along its length and so can react to a large range of sound frequencies [16]. The ability of the ear to amplify incoming sounds is still not understood, and is believed at present to derive solely from active mechanical forcing from *outer hair cells* lying adjacent to the basilar membrane. Fluid-mechanical contributions to this amplification mechanism have not yet been considered, and so we plan to investigate the stability of the basilar membrane and whether resonances can play a role for the parameter values of interest. Modelling the ear's ability to actively amplify sound is necessary in understanding the basic hearing mechanisms, and might also lead to improvements in devices and techniques for mitigating hearing impairments.

Bibliography

[1] John B. Bell, Phillip Colella, and Harland M. Glaz. A second-order projection method for the incompressible Navier-Stokes equations. *Journal of Computational Physics*, 85(2):257–283, 1989.

[2] Richard P. Beyer. A computational model of the cochlea using the immersed boundary method. *Journal of Computational Physics*, 98:145–162, 1992.

[3] Richard P. Beyer and Randall J. LeVeque. Analysis of a one-dimensional model for the immersed boundary method. *SIAM Journal on Numerical Analysis*, 29(2):332–364, 1992.

[4] David L. Brown, Ricardo Cortez, and Michael L. Minion. Accurate projection methods for the incompressible Navier-Stokes equations. *Journal of Computational Physics*, 168(2):464–499, 2001.

[5] Alexandre Joel Chorin. Numerical solution of the Navier-Stokes equations. *Mathematics of Computation*, 22(104):745–762, 1968.

[6] Alexandre Joel Chorin. On the convergence of discrete approximations to the Navier-Stokes equations. *Mathematics of Computation*, 23(106):341–353, 1969.

[7] Ricardo Cortez and Douglas Varela. The dynamics of an elastic membrane using the impluse method. *Journal of Computational Physics*, 138:224–247, 1997.

[8] Ricardo Cortez, Charles S. Peskin, John M. Stockie, and Douglas Varela. Parametric resonance in immersed elastic boundaries. *SIAM Journal on Applied Mathematics*, 65(2):494–520, 2004.

[9] Ricardo Cortez, Nathaniel Cowen, Robert Dillon, and Lisa Fauci. Simulation of swimming organisms: coupling internal mechanics with external fluid dynamics. *Computing in Science & Engineering*, 6:38–45, 2004.

[10] Earl H. Dowell and Kenneth C. Hall. Modeling of fluid-structure interaction. *Annual Review of Fluid Mechanics*, 33:445–490, 2001.

[11] Aaron L. Fogelson. A mathematical model and numerical method for studying platelet adhesion and aggregation during blood clotting. *Journal of Computational Physics*, 56:111–134, 1984.

[12] Boyce E. Griffith and Charles S. Peskin. On the order of accuracy of the immersed boundary method: Higher order convergence rates for sufficiently smooth problems. *Journal of Computational Physics*, 208(1):75–105, 2005.

[13] Matthew M. Hopkins and Lisa J. Fauci. A computational model of the collective fluid dynamics of motile micro-organisms. *Journal of Fluid Mechanics*, 445:149–174, 2002.

[14] Yongsam Kim and Charles S. Peskin. 2-D parachute simulation by the immersed boundary method. *Preprint*, 2001.

[15] Yongsam Kim and Charles S. Peskin. Penalty immersed boundary method for an elastic boundary with mass. *Preprint*, 2005.

[16] Yongsam Kim and Jack Xin. A two-dimensional nonlinear nonlocal free-forward cochlear model and time domain computation of multitone interactions. *Multiscale Modeling and Simulation*, 4(2):664–690, 2005.

[17] K. Kumar and L. S. Tuckerman. Parametric instability of the interface between two fluids. *Journal of Fluid Mechanics*, 279:49–68, 1994.

[18] Ming-Chih Lai and Zhilin Li. A remark on jump conditions for the three-dimensional navier-stokes equations involving an immersed moving membrane. *Applied Mathematical Letters*, 14(2):149–154, 2001.

[19] Long Lee. *Immersed Interface Methods for Incompressible Flow with Moving Interfaces.* PhD thesis, University of Washington, Seattle, WA, 2002.

[20] Long Lee and Randall J. LeVeque. An immersed interface method for incompressible Navier-Stokes equations. *SIAM Journal on Scientific Computing*, 25(3):832–856, 2003.

[21] Randall J. LeVeque and Zhilin Li. The immersed interface method for elliptic equations with discontinuous coefficients and singular sources. *SIAM Journal on Numerical Analysis*, 31(4):1019–1044, 1994.

[22] Randall J. LeVeque and Zhilin Li. Immersed interface methods for stokes flow with elastic boundaries or surface tension. *SIAM Journal on Scientiric Computation*, 8(3):709–735, 1997.

[23] Andrew R. Mitchell. *Computational Methods in Partial Differential Equations.* J. Wiley: London, New York, 1969.

[24] Rajat Mittal and Gianluca Iaccarino. Immersed boundary methods. *Annual Review of Fluid Mechanics*, 37:239–261, 2005.

[25] J. Blair Perot. An analysis of the fractional step method. *Journal of Computational Physics*, 108(1):51–58, 1993.

[26] Charles S. Peskin. Flow patterns around heart valves: A numerical method. *Journal of Computational Physics*, 10:252–271, 1972.

[27] Charles S. Peskin. Numerical analysis of blood flow in the heart. *Journal of Computational Physics*, 25:220–252, 1977.

[28] Charles S. Peskin. Mathematical aspects of physiology. In *Lectures in Applied Mathematics*, volume 19. American Mathematical Society, 1981.

[29] Charles S. Peskin. The fluid dynamics of heart valves: Experimental, theoretical and computational methods. *Annual Review of Fluid Mechanics*, 14:235–259, 1982.

[30] Charles S. Peskin. The immersed boundary method. In Arieh Iserles, editor, *Acta Numerica*, volume 11, pages 479–517. Cambridge Unversity Press, 2002.

[31] Charles S. Peskin and David M. McQueen. Heart simulation by an immersed boundary method with formal second-order accuracy and reduced numerical viscosity. In H. Aref and J.W. Phillips, editors, *Mechanics for a New Millennium, Proceedings of the International Conference on Theoretical and Applied Mechanics (ICTAM)*. Kluwer Academic Publishers, 2001.

[32] Charles S. Peskin and Beth F. Printz. Improved volume conservation in the computation of flows with immersed elastic boundaries. *Journal of Computational Physics*, 105:33–46, 1993.

[33] William H. Press, Saul A. Teukolsky, and William T. Vetterling. *Numerical Receipes in Fortran 77: The Art of Scientific Computing*. Cambridge University Press: Cambridge, New York, 1992.

[34] William H. Press, Saul A. Teukolsky, William T. Vetterling, and Brian P. Flannery. *Numerical Receipes in Fortran 90: The Art of Parallel Scientific Computing*. Cambridge University Press: Cambridge, New York, 1996.

[35] Christine M. Scotii, Alexander D. Shkolnik, Satish C. Muluk, and Ender A. Finol. Fluid-structure interaction in abdominal aortic aneurysms: Effects of asymmetry and wall thickness. *Biomedical Engineering Online*, 4:64, 2005.

[36] John M. Stockie. *Analysis and Computation of Immersed Boundaries, with Application to Pulp Fibers*. PhD thesis, University of British Columbia, 1997. http://www.iam.ubc.ca/theses/stockie/stockie.html.

[37] John M. Stockie and Sheldon I. Green. Simulating the motion of flexible pulp fibres using the immersed boundary method. *Journal of Computational Physics*, 147(1):147–165, 1998.

[38] John M. Stockie and Brian T.R. Wetton. Stability analysis for the immersed fiber problem. *SIAM Journal on Applied Mathematics*, 55(6):1577–1591, 1995.

[39] Gilbert Strang. *Introduction to Applied Mathematics.* Wellesley-Cambridge Press: Wellesley, Mass, 1986.

[40] Cheng Tu and Charles S. Peskin. Stability and instability in the computation of flows with moving immersed boundaries: A comparison of three methods. *SIAM Journal on Scientific Statistics and Computation*, 13(6):1361–1376, 1992.

[41] Luoding Zhu and Charles S. Peskin. Simulation of a flapping flexible filament in a flowing soap film by the immersed boundary method. *Journal of Computational Physics*, 179:452–468, 2002.